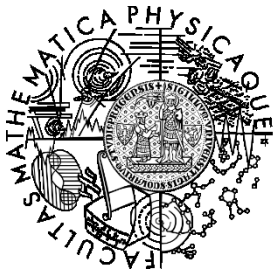

FACULTY
OF MATHEMATICS
AND PHYSICS
Charles University

DOCTORAL THESIS

Tomáš Popelář

Ultrafast laser spectroscopy of semiconductors

Department of chemical physics and optics

Supervisor of the doctoral thesis: prof. RNDr. Petr Malý, DrSc.

Study programme: Physics

Study branch: Optics and optoelectronics

Prague 2022

I declare that I carried out this doctoral thesis independently, and only with the cited sources, literature and other professional sources. It has not been used to obtain another or the same degree.

I understand that my work relates to the rights and obligations under the Act No. 121/2000 Sb., the Copyright Act, as amended, in particular the fact that the Charles University has the right to conclude a license agreement on the use of this work as a school work pursuant to Section 60 subsection 1 of the Copyright Act.

In ……. date ……. …….

Author's signature

First and foremost I would like to thank my supervisor, prof. Petr Malý, for his guidance, inspiration, and immense patience over all those years. I am also very grateful to doc. František Trojánek for the technical support, mainly the creation of the controlling software for the pump and probe measurements, and to Martin Kozák, Ph.D., for the help with results interpretation.

I would like to thank also to my second “research family” at the Institute of Physics of the Czech Academy of Sciences, prof. Ivan Pelant, Lukáš Ondič, Ph.D. and especially Kateřina Kůsová, Ph.D., for their help with experiments on nanocrystalline silicon and interpretation of results.

To all the other colleagues, thank you for all the discussions on related and unrelated subjects.

Last but not least I would like to acknowledge the support of my family without which I would not have the energy and perseverance to do this work.

Název práce: Ultrarychlá laserová spektroskopie polovodičů

Autor: Tomáš Popelář

Katedra: Katedra chemické fyziky a optiky

Vedoucí disertační práce: prof. RNDr. Petr Malý, DrSc., Katedra chemické fyziky a optiky

Abstrakt: Tato disertační práce se zabývá studiem moderních polovodičových materiálů, diamantu a křemíkových nanokrystalů, pomocí metod laserové spektroskopie. Pro detailní výzkum diamantu bylo postaveno nové experimentální uspořádání, generátor laserových pulsů ve střední infračervené oblasti. S jeho pomocí byla zkoumána dynamika excitovaných nosičů o vysokých hustotách, jejich kondenzace do elektron-děrové kapaliny a interakce se světlem kolem jejich plasmové frekvence. Díky vysoké citlivosti těchto měření na teplotu nosičů bylo možné vidět dynamiku termalizace, k jejímuž popisu byla použita kvantová teorie absorpce na volných nosičích.

V dopovaných křemíkových nanokrystalech zabudovaných do SiO_2 matrice jsme zkoumali potenciální přítomnost volných nosičů, která by umožnila vytvořit PN přechod. Dále jsme v těchto vzorcích objevili významný rekombinační kanál, který se projevuje při vysokých intenzitách excitace. Identifkovali jsme jeho původ a popsali jeho interakci s nanokrystaly. Nakonec jsme analyzovali vliv atomů bóru v nanokrystalech na distribuci časů doznívání podle vyzářené vlnové délky.

Klíčová slova: diamant, křemíkové nanokrystaly, časově rozlišená spektroskopie, NBOHC

Title: Ultrafast laser spectroscopy of semiconductors

Author: Tomáš Popelář

Department: Department of chemical physics and optics

Supervisor: prof. RNDr. Petr Malý, DrSc., Department of chemical physics and optics

Abstract: This Ph. D. thesis is focused on the study of modern semiconductor materials, diamond, and silicon nanocrystals, by methods of laser spectroscopy. A new experimental setup, the generator of mid-infrared laser pulses, was built to study diamond in detail. With its help, we observed the dynamics of high-density excited carriers, their condensation into electron-hole liquid, and their interaction with light around their plasma frequency. Thanks to the high sensitivity of these measurements on the excited carrier temperature we could observe the thermalisation dynamics which was described by the quantum theory of free carrier absorption.

In the doped silicon nanocrystals embedded into SiO_2 matrix, we studied the potential presence of free carriers which could be used to create a PN junction. We also found an important recombination channel in these samples which manifests at high excitation intensities. We identified its origin and described its interaction with nanocrystals. At last, we analyzed the influence of incorporated boron atoms on the distribution of decay times according to the emitted wavelength.

Keywords: diamond, silicon nanocrystals, time-resolved spectroscopy, NBOHC

Table of Contents

Introduction

Semiconductors transformed the world at first with novel applications and at second with scalability and cheap fabrication. This was enabled by the primary semiconducting material, silicon, which fortunately has many advantageous properties and is also abundant. The expansion to almost all areas of modern life naturally put forward disadvantages as no one material can be expected to fulfill all the needs adequately. This brought demand for new materials that could fill some of the needs better.

One of the key challenges of today is energy efficiency. Due to the pressure of climate change, a monumental shift from the old dirty energy sources to the new clean ones is underway. This is creating at least temporary energy supply deficiencies among the rising demand for energy due to the rising global standard of living. The new semiconducting materials can help to resolve these issues.

This thesis looks at two such materials, diamond, and nanocrystalline silicon. Diamond being a specific crystalline arrangement of carbon can rival silicon with abundance since the discovery of synthetic fabrication techniques. Having a wide bandgap, it can naturally fill a role in power electronics currently being filled by other wide bandgap materials like GaN and SiC. For example, Mitsubishi SiC MOSFETS reduce the losses compared to Si power devices by 50%. Diamond properties are superior in almost every aspect and it holds great promise in further reducing the losses in energy distribution by 75%. Another application with far-reaching consequences is quantum computing which can reduce energy consumption by a big factor and diamond is one of the prime candidates for qubits.

Nanocrystalline silicon holds the promise of taking advantage of advanced silicon technology and enhancing it with better optical properties. Photonics (i.e. all-optical equivalents of electronic devices) already fulfills the

role of broadband, high-speed, and high-density data interconnects but is held back by no practical solution for an on-chip light source that would brink higher energy efficiency because using off-chip light sources leads to coupling losses. One of the first prospects of nanocrystalline silicon that would solve this issue has been the development of silicon laser, but it is yet unrealized. Another possible and heavily explored prospect is constructing new types of solar cells which would bypass the Shockley-Queisser limit and multiply the efficiency of these photovoltaic devices.

All these advanced applications demand a thorough understanding of the materials on a fundamental level which still has many gaps despite decades of research. In this thesis, we filled some of these gaps primarily by methods of time-resolved spectroscopy, which offer a very sensitive and non-invasive solution to monitoring the dynamics of excited carrier density (transient transmission measurements) and their recombination (streak camera measurements). This way we were able to study the behavior of charged carriers around their plasma frequency, their thermalisation, and interaction with defects repeatedly and reliably in the same samples.

This thesis is divided into four chapters. In the first chapter, we go through the experimental techniques and setups used in our measurements. The second chapter captures building the difference frequency generation setup where we go through the relevant theory, discuss the decision points we went through and calculate the relevant parameters. Then we describe the implementation of said setup into the measuring arrangement which extends its applicability in a unique way.

In the third chapter, we go through our results on the monocrystalline diamond. We focused on the ultrafast dynamics of the excited charge carriers, their condensation into the electron-hole liquid, and modeling the system response by the classical and quantum theory of free carrier absorption. We wanted to study the behavior of charged carrier populations around their plasma frequency for which we used the difference frequency generation setup. The

setup also enabled us to study carrier thermalisation. This part of the work was done in optical laboratories belonging to the Division of Quantum Optics and Optoelectronics of the Department of Chemical Physics and Optics at Charles University.

The fourth chapter is dedicated to the time-resolved photoluminescence of silicon nanocrystals deposited with the presence of boron and phosphorous with the prospect of generating free electrons and holes to realize a PN junction. We wanted to study if the free carriers are present and their effect on photoluminescence. This part of the work was conducted in a laboratory belonging to the Department of Thin Films and Nanostructures at the Institute of Physics of the Czech Academy of Sciences.

1 Experimental setups

Our experimental considerations have concentrated on the study of ps-ms processes in our semiconducting samples. Such a wide timescale cannot be encompassed by one method and more approaches are necessary. In this chapter, we will describe the particularities of each approach and the general results which can be expected of them.

1.1 Time-resolved photoluminescence using a streak camera

There is a multitude of approaches how to measure time-resolved photoluminescence (TRPL) with gating methods like up-conversion and time-correlated single-photon counting or using special detectors like photomultiplier, iCCD, or streak camera among many others. All methods have their advantages and disadvantages, the TRPL setup used in this work utilizes a streak camera for detection. The main advantage of this method is a very good time-resolution (as high as few ps) and range (ns-s) as well as ease-of-use and fast data collection in addition to general photoluminescence (PL) advantages which are non-invasiveness and high sensitivity. The main disadvantage is a low dynamic range – the PL has to be sufficiently weak to produce undistorted data.

The principle of the streak camera is reproduced in **Fig. 1.1**. In short, streak camera setup works as follows:

PL is collected into a spectrograph where the light is spatially separated according to the wavelength. This light is then input into a streak unit (the left-most point in **Fig. 1.1**) through an input slit. There it is first converted to electrons. These electrons are then accelerated and swept along the vertical axis by an electric field. This electric field ramps in time which gives a time

resolution to the vertical axis. These electrons are converted back to photons which are detected by a CCD camera. There may be an amplification stage in front of the camera.

The time resolution depends on several factors. The first is geometric – since the time information is converted into the spatial one, the width of the input slit affects the resolution similarly like a wavelength resolution is affected by an input slit in spectrograph. This is directly connected to the resolution given by a time window – the longer the window the lower the resolution is. Longer time windows require a longer gating electric field to contain all the electrons in that window and to accommodate them on the vertical axes limited by the size of a CCD the strength of the field needs to be weaker. The electrons are thus swept less and more of them coincide on the same pixel. For short time windows, the resolution is limited by the width of the light strip, for time windows longer than 10 ns the limitation is the size of the pixels – the time resolution is then linearly dependent on the chosen time window as can be seen in **Fig. 1.2**.

Another important factor for the measurement is a low level of incoming light – the detection system is tailored for a single-photon counting regime. This means that light detected on a pixel is registered as a 1 during the integration period (therefore it is advantageous to match this period to a camera read-out frequency limit to obtain the most signal in the shortest time). For the system to behave linearly there must be a very low probability for two or more photons impacting one pixel during a particular integration period. If the percentage of activated pixels during measurement does not exceed 5% in an area of the highest detected intensity, this condition should be sufficiently fulfilled.

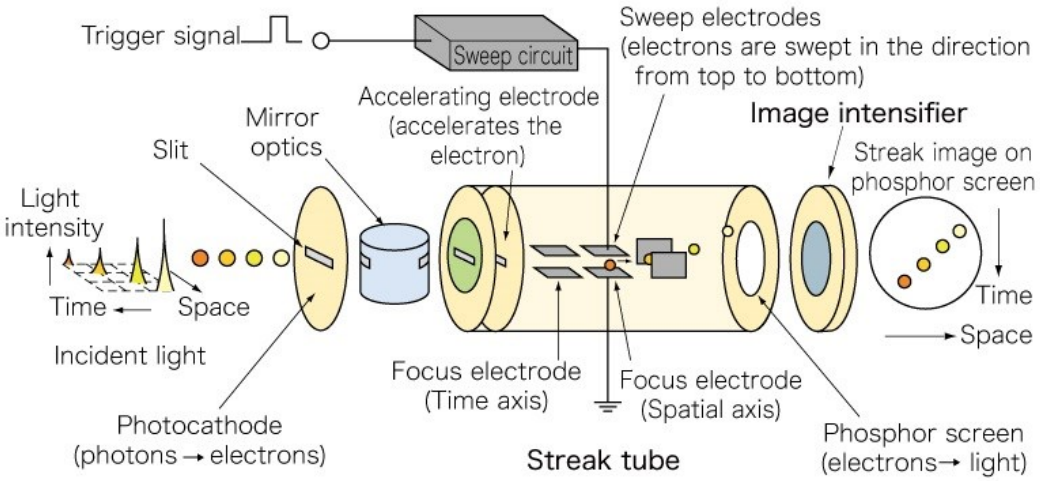

Fig. 1.1 Schematic principle of a streak camera (after [1]). The incident light is already dispersed on the horizontal axis by a monochromator before entering the streak unit. The photons are converted on photocathode to electrons which are accelerated and swept along the vertical axis in the streak tube by a ramping electric field. This makes the electrons arriving later be further down. The electrons are then multiplied in the microchannel plate and converted back to photons in the phosphor screen. The resulting photons are detected by a CCD camera.

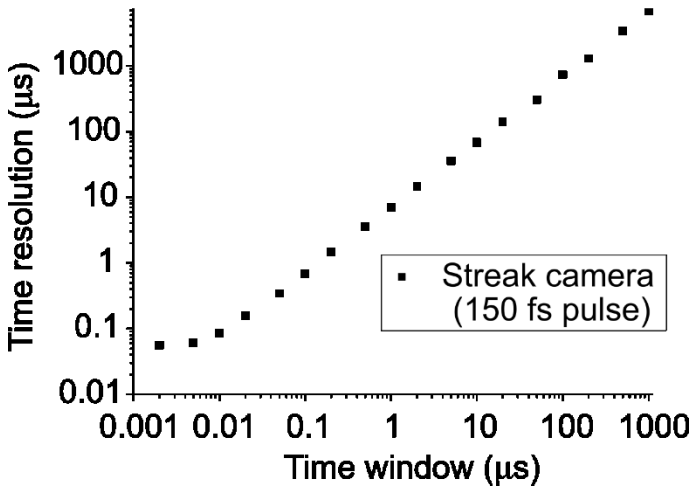

Fig. 1.2 Time resolution of the streak camera dependence on the measurement time window in a log-log scale. A 150 fs laser pulse was used as a "delta" function, i.e. pulse with infinitely narrow time length.

Devices used in this arrangement were monochromator Acton SpectraPro SP2330 and streak camera Hamamatsu C10627. The camera was calibrated by white calibration lamp Oriel and all the PL spectra were corrected to the measured spectral sensitivity.

Excitation was done by a frequency tripled output of femtosecond laser PHAROS (Light Conversion) with 150 fs pulses at 1 kHz repetition frequency and fundamental wavelength 1030 nm. The conversion to 343 nm was done in harmonic generator HIRO (Light Conversion).

1.2 Pump and probe setup (P&p)

This experimental setup monitors the dynamics of the charge carriers population in the sample. The main advantage is universality and supreme time resolution. The basic consists of two beams – a stronger one called a pump which is used to excite the sample and a weaker one (sufficiently weak not to disturb the system) to detect the changes in either the transmission or reflection of the sample. Depending on the chosen beams, one can very selectively choose what carrier populations are excited and which processes to monitor. We used exclusively a setup that observed the transient transmission ΔT of the probe beam, thus we will describe this variant particularly, but the description can be applied also to a reflectivity case. The changes in transmission were determined by comparing the transmission of the probe beam passing through the excited sample T_{exc} to the transmission after the unexcited sample T_0:

$$\frac{\Delta T}{T_0} = \frac{T_{exc} - T_0}{T_0} \tag{1.1}$$

A schematic of such an arrangement is in **Fig. 1.3**. The time resolution is supplied by a delay line with a retroreflector which changes the path length of one of the beams. The time resolution limit is given by the convolution of the smallest step of the delay line and the length of the laser pulse.

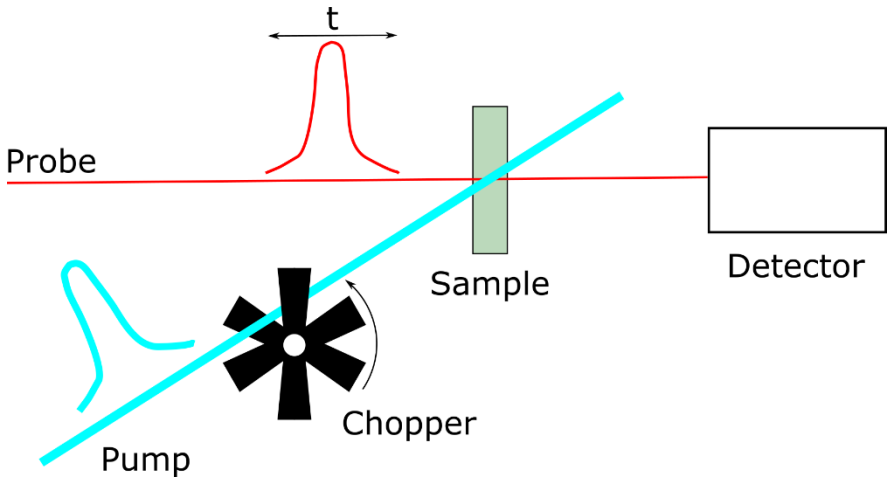

Fig. 1.3 Schematic of a basic P&p setup. Beams overlap in the sample and changes in the intensity of the probe beam due to the excitation by the pump beam are recorded in the detector. These changes are recorded dependent on the relative time delay between the two beams. A chopper forces a different repetition frequency of the pump to compare the response of the excited to the unexcited sample.

Since the changes in transmission can be very small (0.01 – 0.1 %), demands on alignment and sensitivity are large. To improve the sensitivity or more precisely the signal-to-noise ratio, there are more avenues to explore. Firstly the probe beam should be as intense as possible complying with a condition to not disturb the system too much compared to the pump beam. This setup can be generally distinguished into two cases – probe and pump have the same or different wavelength – in the former case the intensity ratio of 1:10 between the two beams is sufficient, in the latter case it depends on the response of the unexcited system to a particular wavelength.

Secondly one can filter out the fluctuations of intensity of the pump/probe beams by referencing the actual intensity of the beam just before the detection. This is achieved by splitting the small portion of the beam onto a second detector. Another avenue is to force the signal to be of a particular frequency and filter out any signal which is “out of sync”. This is achieved by using a chopper in a pump beam and using a lock-in amplifier.

Another option, which was used in our case with the mid-infrared (MIR) probe beam, is a “classical” one – averaging over many measurements. This is a suboptimal solution since it is time-intensive, but it is always available. The intensity of our MIR probe beam was unfortunately too low to get sufficient detector output for the lock-in amplifier to function properly.

2 Building the P&p setup utilizing MIR pulses

In this chapter, we will describe the steps we used to build an experimental setup that generates MIR pulses and uses them as the probe beam to measure transient transmission. We will start with a description of possibilities in the MIR generation and the actual solution used. We will then give a brief overview of difference frequency generation (DFG) theory and how it translated into our solution. Lastly, we will describe the actual P&p setup using MIR pulses. This is quite a unique extension that is as we will show in chapter 3 extra sensitive to the processes we were interested in observing, namely free carrier absorption and thermalisation. The main disadvantage is added difficulty to the experimental design because the ambient atmosphere readily absorbs the vast part of the MIR range, which is also invisible to the common cameras making alignment in such a sensitive setup challenging.

2.1 Experimental realization of generating MIR pulses

To achieve laser pulses in the MIR range there are two possibilities – direct source and indirect generation through nonlinear interaction. There are several direct sources like quantum cascade [2] or lead-salt lasers [3]. These sources are limited in power, pulse duration, and tunability.

Nonlinear interactions available to generate pulses in the MIR range are supercontinuum and difference frequency generation. Supercontinuum lasers [4] are now readily available with high power, short pulses, and broad range, but rarely do we get a good combination of all these parameters. A big advantage is that the whole generated range is available at once (in cases where it is undesirable bandpass filters are used) without further adjustments.

Difference frequency generation (DFG) is a more complicated but more flexible setup and with a sufficiently powerful laser also a cheaper solution. The first choice is the nonlinear crystal for a generation. There are many options: Silver Thiogallate ($AgGaS_2$, AGS), Silver Gallium Selenite ($AgGaSe_2$), Gallium Selenide (GaSe), etc. We chose AGS crystal which has a bit limited generation range (3 - 10 μm) and has a lower damage limit. But its advantage is that it is atmospherically and mechanically stable, in short durable.

DFG was realized between *signal* and *idler* beams from the parametric amplifier TOPAS (Light Conversion). Due to the different optical path lengths of these two beams, the idler and signal pulses are not coincident. To remedy this these two beams need to be split into two different paths which can be time-shifted relatively to each other (through a delay line) and rejoined in the crystal. The splitting was done by dichroic mirrors supplied by the manufacturer of TOPAS, but we had to find our solution for rejoining. The easiest solution would be (after necessary path adjustment) to send the beams directly into the crystal. The efficiency of generation would suffer because the interaction length would be short. To achieve the highest possible efficiency the beams need to be parallel.

We exploited the fact that beams are cross-polarized (signal has vertical polarization, idler horizontal) and rejoin them the on Glenn-Taylor polarizer. This component is primarily used for light polarization producing two cross-polarized beams (ordinary and extraordinary), but if we replace the output as an input we can use it to make the beams parallel (**Fig. 2.1**).

The crystal was placed into a gimbal mount which rotates the crystal along a horizontal axis without any translation. The mounting also lets the crystal rotate around the axis perpendicular to its surface. These two degrees of freedom are sufficient to tune the DFG effectivity since AgS is a uniaxial nonlinear crystal.

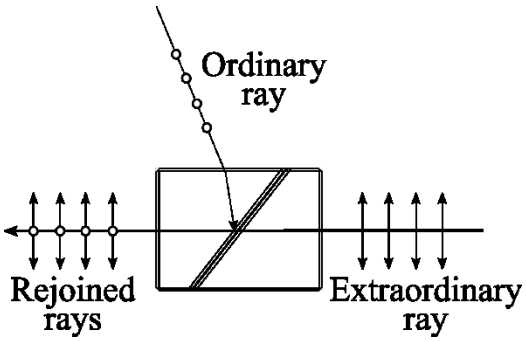

Fig. 2.1 Schematic of Glenn-Taylor polarizer used to rejoin the signal and idler beams. The beams exit the polarizer coinciding in time and space. The rays are cross-polarized (arrows, open dots).

2.2 Theory of difference-frequency generation

The complete theory can be found in [5] and [6] so we will list only the necessary equations to establish the mechanism of DFG. It is three-wave non-degenerate interaction where two waves (with frequencies ω_1 and ω_2) are interacting with each other in a non-linear medium and produce a third wave with frequency $\omega_3 = \omega_1 - \omega_2$. Other non-linear interactions which can happen for these beams are second harmonic generation and sum-frequency generation. Selection between these interactions is realized by phase matching conditions – all three waves must "travel at the same speed" for the interaction to be the most efficient. This means that the original waves add coherently into producing the third wave and the most energy is extracted.

The polarizability of a medium P can be rewritten into the following general series:

$$\begin{aligned} P = P_1 + P_{NL} &= P_1 + P_2 + P_3 + \cdots \\ &= \varepsilon_0\left(\chi^{(1)}E + \chi^{(2)}E^2 + \chi^{(3)}E^3 + \cdots\right) \end{aligned} \tag{2.1}$$

where P_1 is a linear part of polarizability, P_{NL} the nonlinear part, ε_0 vacuum permittivity, $\chi^{(\mathrm{i})}$ ith-order tensor of susceptibility, and E electric field. We will

be interested only in the second term, P_2, which governs the interaction of two beams. If the electric field consists of two frequency components ω_1 and ω_2, it can be written as:

$$E(t) = E_1 e^{-i\omega_1 t} + E_2 e^{-i\omega_2 t} + E_1^* e^{i\omega_1 t} + E_2^* e^{i\omega_2 t} \tag{2.2}$$

Inserting (2.2) into (2.1) we get several non-linear contributions with different combinations of ω_1 and ω_2. DFG is described by:

$$\begin{aligned} P(\omega_3 = \omega_1 - \omega_2) &= 2\varepsilon_0 \chi^{(2)} E_1 E_2^* e^{-i\omega_3 t} \\ &= 2\varepsilon_0 \chi^{(2)} A_1 e^{-ik_1 z} A_2^* e^{ik_2 z} \end{aligned} \tag{2.3}$$

where A_1, A_2 are time-dependent amplitudes of the electric field, k_1, k_2 wavevectors, and z is space coordinate in the direction of propagation. The second-order tensor of electric susceptibility $\chi^{(2)}$ reduces for a fixed geometry, i.e. fixed propagation and polarization directions to:

$$\chi^{(2)} = 2d_{eff} \tag{2.4}$$

where the angles between the propagation of the waves and crystalline axis as well as the polarization of the waves define the formula for effective nonlinearity d_{eff}. It depends on the specific nonlinear interaction and used crystal and will be shown later.

In **Fig. 2.2** we show a schematic of the interaction in the medium. When we input (2.2) and (2.3) into Maxwell equations we get the following expressions for the propagation of the 3 waves:

$$\frac{\mathrm{d}^2 A_n}{\mathrm{d}z^2} + 2ik_n \frac{\mathrm{d}A_n}{\mathrm{d}z} = \frac{-4d_{eff}\omega_n^2}{c^2} A_m A_l e^{i(k_m + k_l - k_n)z} \tag{2.5}$$

where c is the speed of light. Indices l, m, n have values 1, 2 or 3 and also $l \neq m \neq n$ that leads to three coupled equations, which must be solved together.

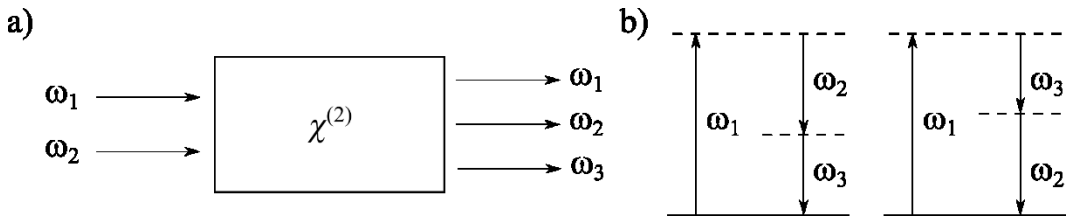

Fig. 2.2 a) Schematic of the DFG in the medium. b) Energy diagram of the interaction with two possible symmetries. Dashed lines are virtual energy levels.

If we consider that the ω_1 wave is not significantly depleted during the interaction ($A_1(z) = A_1(0)$) then we have two equations to solve:

$$\begin{aligned} \frac{\mathrm{d}A_2}{\mathrm{d}z} &= \frac{2id_{eff}\omega_2^2}{k_1c^2}A_1A_3^*e^{i\Delta kz} \\ \frac{\mathrm{d}A_3}{\mathrm{d}z} &= \frac{2id_{eff}\omega_3^2}{k_2c^2}A_1A_2^*e^{i\Delta kz} \end{aligned} \tag{2.6}$$

where $\Delta k = k_1 - k_2 - k_3$.

Let us note that even though the efficiency of the interaction is low thus ω_2 does not deplete either, we cannot set A_2 as constant because A_2 is actually amplified during the interaction as will be shown below.

The general solution of (2.6) is as follows:

$$\begin{aligned} A_2(z) &= \left[A_2(0)\left(\cosh gz - \frac{i\Delta k}{2g}\sinh gz\right)\right. \\ &\qquad \left. + \frac{\kappa_2}{g}A_3^*(0)\sinh gz\right]e^{i\Delta kz/2} \\ A_3(z) &= \left[A_3(0)\left(\cosh gz - \frac{i\Delta k}{2g}\sinh gz\right)\right. \\ &\qquad \left. + \frac{\kappa_3}{g}A_2^*(0)\sinh gz\right]e^{i\Delta kz/2} \end{aligned} \tag{2.7}$$

where $g = [\kappa_2\kappa_3^* - (\Delta k/2)^2]^{1/2}$ and $\kappa_l = \frac{2id_{eff}\omega_l^2A_1}{k_lc^2}$.

The efficiency of all nonlinear interactions is highest in the case of the perfect phase-matching, Δk = 0, the solution then takes the following form:

$$A_2(z) = A_2(0)\cosh\sqrt{\kappa_2\kappa_3^*}z$$
$$A_3(z) = i\left(\frac{n_2\omega_3}{n_3\omega_2}\right)^{1/2}\frac{A_1}{|A_1|}A_2^*(0)\sinh\sqrt{\kappa_2\kappa_3^*}z \quad (2.8)$$

Since *cosh* and *sinh* are rising functions, both lower frequency waves are amplified during the non-linear process. This can be understood intuitively from **Fig. 2.2b**. The depicted process can actually function without the input wave ω_2 – this would be called parametric generation. Turning the nonlinear crystal in this case changes the wavelengths of the two output waves. The presence of wave ω_2 in the case of DFG greatly enhances the efficiency of wave ω_3 generation. But as can be seen from the symmetry in **Fig. 2.2b**, the presence of wave ω_3 must stimulate the generation of wave ω_2. Hence there is the amplification of both waves.

The most efficient way to achieve the perfect phase matching is to use a birefringent crystal, i.e. crystal with different refractive indices, n_o and n_e, according to polarization. The waves experiencing n_o or n_e are called ordinary or extraordinary waves, respectively. There are altogether 4 combinations of wave polarizations which are divided into so-called Type I and Type II conditions: the lower frequencies (ω_2 and ω_3) have the same (Type I) or orthogonal (Type II) polarizations. Since the highest frequency has to have lower of the two refractive indices, only three combinations are viable. In our case, the $n_o > n_e$ and the only possibility for Type I is a combination of n_e (ω_1), n_o (ω_2), and n_o (ω_3). For Type II either ω_3 or ω_2 can be the extraordinary wave. The phase matching is achieved by turning the crystal since n_e changes between n_o and the principal value $\bar{n}_e$ according to the angle θ between the wave propagation vector and crystal axes:

$$\frac{1}{n_e(\theta)^2} = \frac{\sin^2\theta}{\bar{n}_e^2} + \frac{\cos^2\theta}{n_o^2} \tag{2.9}$$

Our crystal is cut most advantageously for DFG meaning that the angle our crystal needed to be turned to achieve the perfect phase-matching is minimal. That is important to maintain the largest aperture possible. The indices of refraction are calculated from Sellmeier equation $n^2 = A + B / (1 - C / \lambda^2) + D / (1 - E / \lambda^2)$. The coefficients A – E with other important parameters of our AGS crystal are in **Table 2.1**.

d_{eff} in our geometry is computed as follows:

$$\begin{aligned} d_{eff} &= d_{36} sin(\theta) && (Type\ I) \\ d_{eff} &= d_{36} sin(2\theta) * cos(2\varphi) && (Type\ II) \end{aligned} \tag{2.10}$$

where φ is the second angle defining the crystal axis direction. The waves ω_1 and ω_2 are bound by the following condition given by the generation of our input waves in a parametric amplifier:

$$\frac{2\pi c}{\lambda_s} = \omega_1 + \omega_2 \tag{2.11}$$

where λ_s = 800 nm is the wavelength of the input beam.

We calculated the perfect phase-matching angle, $d_{eff,}$ and clear aperture for all three combinations of DFG. The clear aperture S is calculated as follows:

$$S = S_{max} \cos\vartheta \tag{2.12}$$

where S_{max} is a maximal aperture given by the crystal size and ϑ is the angle between the surface and the input beam propagation.

Results are in **Fig. 2.3** and **Fig. 2.4**. We can see that for our crystal the Type II interaction with extraordinary DFG wave, DFG (e), is the best. DFG (o)

is mostly unusable since the waves cannot be phase-matched for $\lambda > 5$ μm and Type I has lower $d_{eff.}$

φ	45°	θ	39°	d_{36}	23.6 pm/V
Sellmeier coeff.	A	B	C	D	E
n_o	3.397	2.3982	0.09311	2.164	950
n_e	3.5873	1.9533	0.11066	2.3391	1030.7

Table 2.1 Parameters of the AGS crystal relevant to DFG. Angles φ and θ are inner angles between the optical axis and the crystal surface given by the crystal cut.

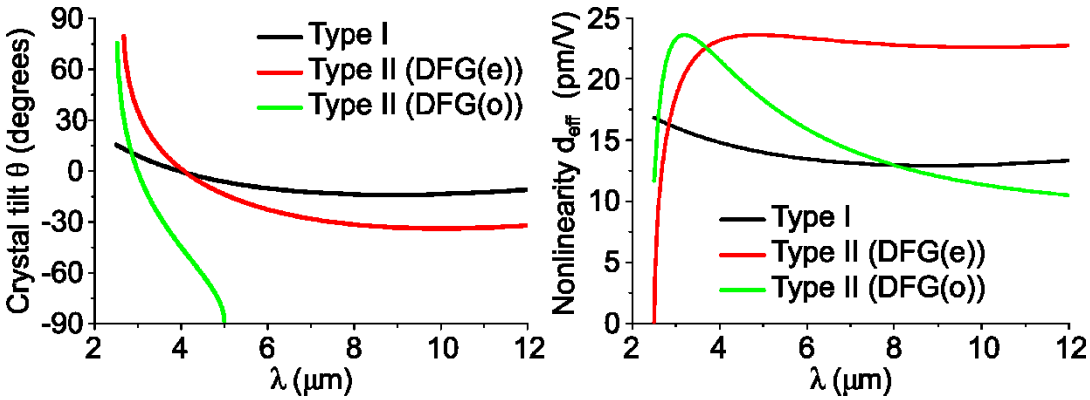

Fig. 2.3 *Left* – Angle of perfect phase-matching based on the generated wavelength. *Right* – Effective non-linearity based on the generated wavelength.

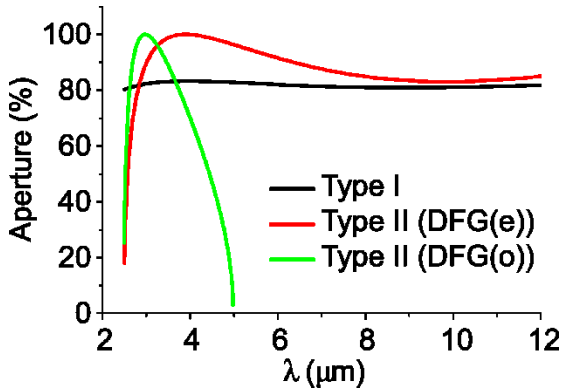

Fig. 2.4 Clear aperture based on the generated wavelength. Shown in the percentage of the maximal aperture. The high percentage is given by the advantageous crystal cut.

2.3 Practical realization of P&p experiment with MIR pulses

The actual setup is in **Fig. 2.5**. The signal collection was realized by thermoelectrically cooled HgCdTe (MCT) detector J15TE4 from the company Teledyne with maximum detectivity at 8.14 μm. To ensure stability and low noise level, the detector was powered by a homemade battery. The laser system was from Spectra-Physics consisting of the seed laser Tsunami which was amplified in Spitfire amplifier producing mJ laser pulses with 100 fs pulse length at 800 nm with a fixed repetition frequency of 1 kHz. This output beam was split into two branches where it underwent frequency conversions as was needed for a particular application.

Since this setup was used to conduct experiments on diamond samples, we used a previously built homemade setup to generate the 4th harmonics of the fundamental pulse, i.e. 200 nm (6.2 eV) in the excitation branch. Despite nominally low pulse energy (~100 pJ) on the output, the samples are excited sufficiently because the photon energy is well above the diamond indirect bandgap (5.49 eV). A delay line was used in this branch due to more stringent alignment requirements in the other branch. A mechanical chopper was also

inserted into this branch, its frequency of 500 Hz was synchronized with the laser.

In the probe branch, two near-infrared beams were generated in parametric amplifier TOPAS in the wavelength range between 1200 – 2700 nm. They were used to generate the MIR probe beam in the wavelength range of 3 – 10 μm as described above.

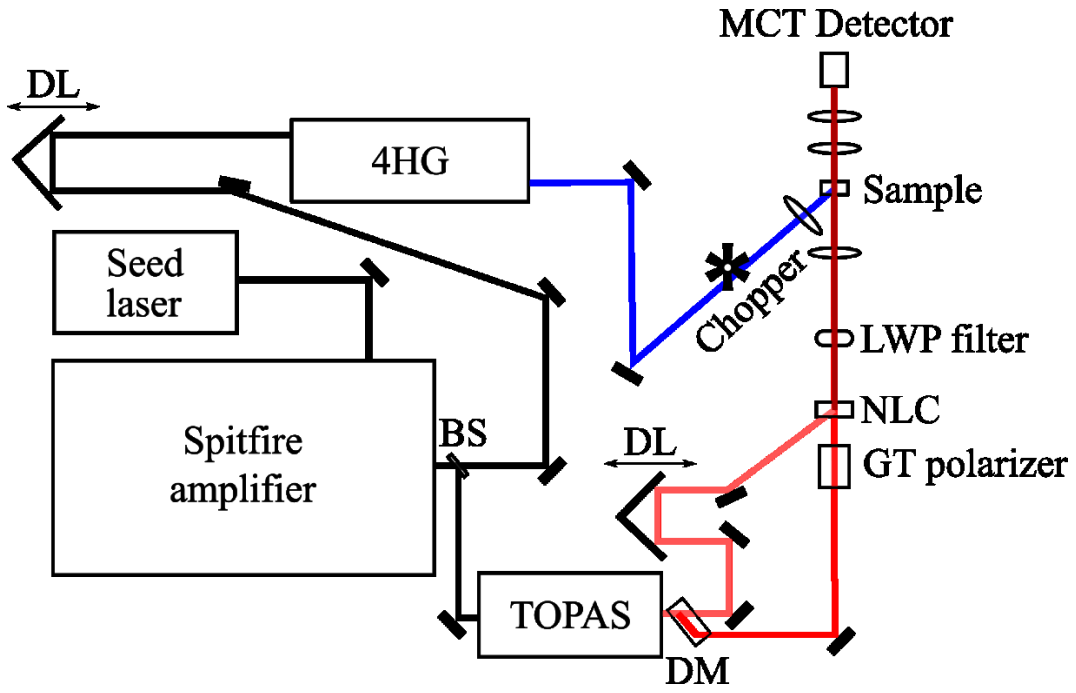

Fig. 2.5 Our transient transmission setup with MIR probe beam. Full rectangles = mirror, Ovals = lenses, BS = beam splitter, DM = dichroic mirror, GT polarizer = Glenn-Taylor polarizer, NLC = non-linear crystal, LWP = long-wave pass filter, DL = delay line. Seed laser supplies the Spitfire amplifier with fs pulses at MHz repetition frequencies. The amplifier output repetition frequency is only 1 kHz, but the pulse energy is in mJ. One part of the output is converted to 200 nm in the 4th harmonics generator (4HG). The second part is converted to IR pulses in an optical parametric amplifier (TOPAS). By the nature of the generation, it creates two collinear beams which are separated by DM and then overlapped in time and space in NLC. The fundamental wavelengths are filtered out by the LWP filter.

The changes in probe beam transmission through the sample were detected by the following method. The output of the MCT detector was taken by AD/DA PC card. By the nature of mechanical chopper frequency being half of laser repetition frequency, the difference between the two subsequent pulses monitors the transient transmission. For every time delay, this difference was recorded many times to enhance the signal-to-noise ratio.

To determine the wavelength of the probe beam, we redirected the beam into a grating monochromator behind which we placed our MCT detector. Technically, we should be able to determine the MIR wavelength just by selecting the right input wavelengths and then tuning the crystal angle to get the maximal signal on the detector. But due to the uncertainties of the TOPAS output wavelengths magnified by their broad spectrum (inherent to ultrashort pulses) and influence of the ambient atmosphere absorption, the probe wavelength needs to be checked every time we adjust the crystal.

We show examples of the MIR pulses recorded by the monochromator in **Fig. 2.6**.

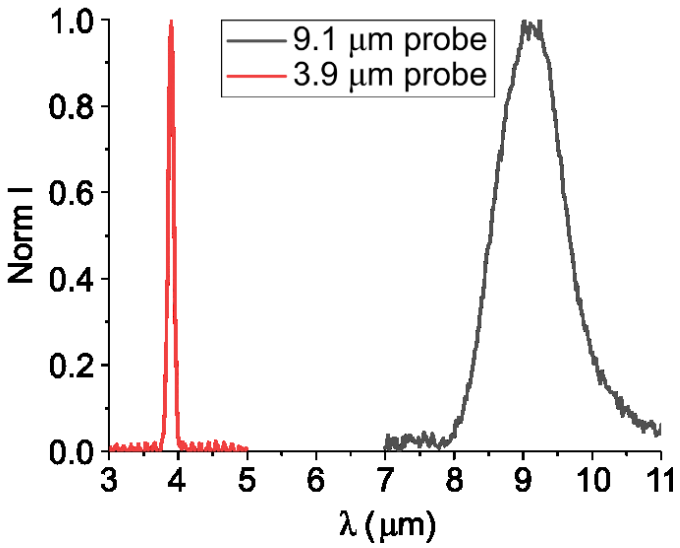

Fig. 2.6 Examples of the probe beam pulses. The apparent broadening is given by the fact that if the two beams have roughly the same duration, they have roughly the same spectral width (in the frequency space). In the wavelength space that translates into broader pulses for longer wavelengths.

3 Crystalline diamond

In this chapter, we will present our results from the measurement of transient transmission in diamond with the MIR probe beam. We will start with a general material overview and introduction to the electron-hole liquid phenomenon. Then we will show our results at low temperatures where we study the response of electron-hole liquid around its plasma frequency. We will conclude with our results at moderate temperatures where we adapt the quantum theory of free carrier absorption to show the usefulness of our MIR probe beam in monitoring excited carrier thermalisation. The results in this chapter were published in [7].

3.1 Material properties

Diamond is carbon arranged into a specific lattice. It has superb mechanical properties (highest hardness and thermal conductivity) which have been exploited in the industry for a long time. But in the past 25 years, the interest shifted to semiconductor applications even though it has a high bandgap of 5.47 eV due to the newly found way of an n-doping diamond by phosphorus in 1996 [8] (p-type doping by boron was established in 1989 [9]). In theory, every semiconducting device like diode or transistor can be made now, but its applications are limited due to the high activation energies of diamond dopants – around 0.37 eV for boron [10], 0.55 eV for phosphorus [11] – the conductivity is still very low at room temperature. On the other hand, diamond possesses the highest carrier mobilities (4500 $cm^2V^{-1}s^{-1}$ for electrons, 3800 $cm^2V^{-1}s^{-1}$ for holes ([12], [13]) when the carriers are freed by external excitation. All these attributes make diamond an excellent material for high-temperature and high-voltage applications ([14], [15]). The last hurdle for diamond applications is the cost-effective manufacturing of large wafers, but there have been made many

advances in recent years ([16], [17]). There are two methods nowadays of diamond manufacturing: HPHT (high pressure, high temperature) which simulates the natural way of diamond creation in volcanos and was developed 70 years ago [18], and CVD (chemical vapor deposition) developed around the same time [19]. HPHT produces high-quality diamonds, but it is expensive and cannot produce big wafers. CVD method is much more flexible, and even though it suffered from quality issues at the start, nowadays, electronic grade CVD diamonds are easily available, and the CVD method is used to produce diamonds on various substrates, doped by impurities, etc. Some diamond devices have been manufactured like UV LEDs [20], high-energy-particle detectors [21], and Schottky diodes [15] among others.

Diamond is an indirect semiconductor with a minimum of the conduction band at 76% distance between Γ and X points in the Brioulline zone, see also **Fig. 3.1a**. Being an indirect semiconductor basic absorption and emission of light must be accompanied by interaction with phonons, thus also a phonon structure is important. The phonon dispersion lines are in **Fig. 3.1b**. The diamond band structure is similar to the Si having 6 equivalent electron minima and 2 equivalent hole maxima. The latest measurements of effective masses of charge carriers are in **Table 3.1**. [22]

Electron mass		Hole mass	
m_t	0.280	m_{lh}	0.260
m_l	1.560	m_{hh}	0.667
m_{de}	0.496	m_{so}	0.375
		m_{dh}	0.947

Table 3.1 Effective masses of charge carriers in diamond.

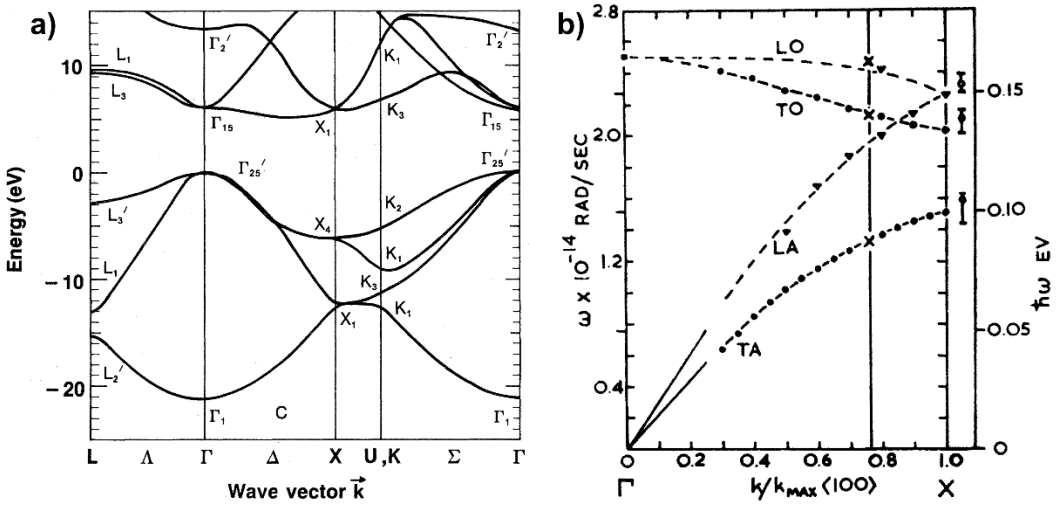

Fig. 3.1 a) Band structure of diamond [23]. b) Phonon dispersion curves of diamond [24]. The line at 0.76 intersects the phonon branches at energies and momentum where they interact with photons and electrons at conduction band minima.

3.2 Electron-hole liquid in diamond

Electron-hole liquid (EHL) is the quantum state of high-density electrons and holes which emerges from the phase transition of dense exciton gas of low temperature to a metallic liquid. It was first predicted by Keldysh [25] and observed by Haynes in silicon [26] though wrongly interpreted as biexciton luminescence. By subsequent theoretical analysis, it was found that for idealized case of non-degenerate bands the molecular phase is more stable than the metallic phase, but in the real case of silicon and germanium, the metallic phase was more stable [27].

For the stability of the EHL, the anisotropy and degeneracy of the bands are essential. Ground state energy E_G can be written as follows:

$$E_G = E_K + E_{exch} + E_{corr} \tag{3.1}$$

where E_k, E_{exch}, and E_{corr} are kinetic, exchange, and correlation energy, respectively. Kinetic energy can be expressed as [28]:

$$E_k = \frac{2.21}{r_s^2}\left(\frac{\mu}{{v_c}^{2/3} m_{de}} + \frac{\mu}{\left(m_{hh}^{3/2} + m_{lh}^{3/2} + m_{so}^{3/2}\right)^{2/3}}\right) \tag{3.2}$$

where r_s is interparticle spacing, v_c number of conduction band minima, μ reduced exciton mass, m_{de} effective mass of electron density of states, and $m_{hh}(m_{lh})$ heavy (light) holes mass. The kinetic energy is the energy "price" given by the localization of carriers in the liquid which must be sufficiently compensated by E_{exch} and E_{corr} for the EHL to be stable. The term in brackets of (3.2) is due to the degeneracy and anisotropy of the bands and it lowers E_k three times ($E_k = 0.7/r_s^2$). It should be noted that this result is based on new sets of electron and hole masses; in [28] E_k was determined as $0.8/r_s^2$ based on the masses in [29].

Exchange energy was derived to be $-1.19/r_s$ and correlation energy $0.4032 \times \ln(r_s - 0.31) - 0.9704$. These expressions lead to quite accurate predictions of experimentally determined parameters of EHL like the density of charge carriers, binding energy, and chemical potential. These are determined indirectly from photoluminescence by fitting the EHL band with the following expression [30]:

$$I_{EHL} \approx \int_0^{\overline{h\upsilon}} \sqrt{E}\sqrt{\overline{h\upsilon} - E}\left[exp\left(\frac{E - F_e}{k_B T}\right) + 1\right]^{-1} \times \left[exp\left(\frac{\overline{h\upsilon} - E - F_h}{k_B T}\right) + 1\right]^{-1} dE \tag{3.3}$$

where F_e (F_h) are Fermi energies for conduction (valence) bands, T temperature of the charge carriers and k_B the Boltzmann constant and:

$$\overline{h\upsilon} = h\nu + \hbar\omega - E_{rg} \tag{3.4}$$

where $h\nu$ is the energy of the emitted photon, $\hbar\omega$ phonon energy, and E_{rg} reduced bandgap energy (the bandgap shrinks due to the high density of charge carriers). The density of charge carriers enters the equation (3.3) through Fermi energies (their sum is also equal to the chemical potential) in charge-neutrality condition:

$$n_0 = n_e = n_h = \\ = \frac{v_{c(h)}\left(2m_{de(h)}\right)^{3/2}}{2\pi^2\hbar^3}\int_0^{\infty}\sqrt{E}\left[exp\left(\frac{E-F_{e(h)}}{k_BT}\right)+1\right]^{-1}dE \quad (3.5)$$

The EHL was predicted in diamond as long ago as in 1979 [31], but the first experimental evidence was measured in 2000 [32]. The reason for such a delay was a lack of a strong enough excitation source that would not heat diamond significantly. Diamond has been traditionally studied by cathodoluminescence which easily has sufficient energy to excite electrons over the bandgap. Unfortunately, it apparently heats the lattice too much despite deep cooling. The optical excitation systems are thus essential to study EHL in diamond.

Many more experiments with EHL were done since then. The phase diagram was determined experimentally and theoretically on the low-density side in [33] and high-density side in [34] with critical temperature T_c = 165 K and critical density $n_c = 1\times10^{20}$ cm^{-3} (**Fig. 3.2**), i.e. the maximum charge carriers temperature for them to undergo condensation and their minimal density in EHL. It was found that EHL can be manipulated by applying stress leading to suppression of condensation due to lifting the conduction band degeneracy leading to rising of E_k [35]. On the other hand, condensation can be enhanced by exciting the sample again shortly after primary excitation [36]. Or the drops can be evaporated leading to secondary condensation since the right physical conditions are still there [37].

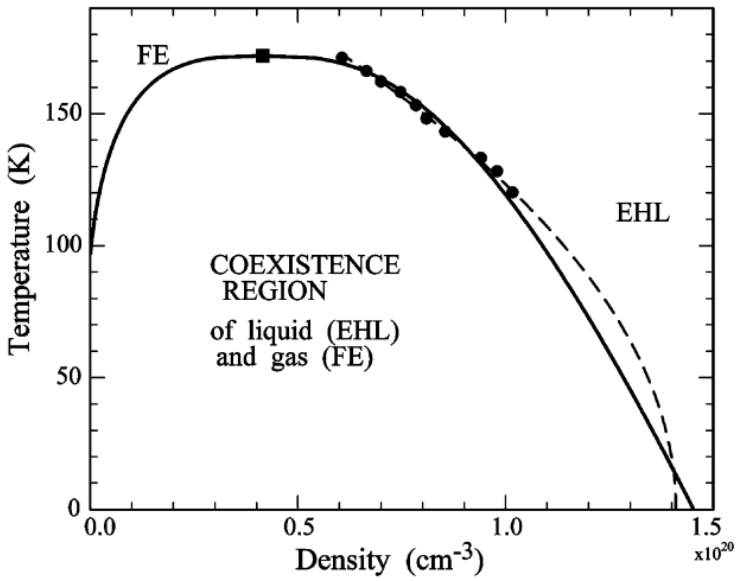

Fig. 3.2 Phase diagram of EHL and free-exciton gas. After [38]. Solid line – fit by empirical Guggenheim model with critical point [n_c, T_c] (square). Dashed line – fit by degenerate plasma model. Circles – experimental points.

3.3 Drude theory

In our case, the signal detected in the P&p setup is due to the free carrier absorption (FCA) which can be effectively described by classical Drude theory [39]. It is relatively simple but still gives quite accurate results when its conditions are fulfilled and no magnetic field is applied. The electrons are considered free and change their states only through collisions with an immobile background. Other interactions are neglected. Drude theory can be considered empirical since it does not presuppose a concrete scattering mechanism.

From the general expression of damped oscillation of charge e electric field E(t) $m\ddot{x} + m\Gamma\dot{x} - \omega_0^2 x = eE(t)$ setting ω_0 at zero (no resonance), we get the following solution:

$$x = \frac{eE}{m(\omega^2 + i\Gamma\omega)} \tag{3.6}$$

where Γ is scattering frequency. The polarization caused by the presence of free carriers with concentration n_c, $P_{FC} = -en_c x$, gives rise to susceptibility χ_{FC}:

$$\chi_{FC} = \frac{P_{FC}}{\varepsilon_0 E} = \frac{ne^2}{m^* \varepsilon_0 (\omega^2 + i\Gamma\omega)} = \frac{\omega_p^2}{(\omega^2 + i\Gamma\omega)} \tag{3.7}$$

where ω_p is plasma frequency defined as:

$$\omega_p{}^2 = \frac{e^2 n_c}{\varepsilon_0 m^*} \tag{3.8}$$

where m^* is the effective mass of free carriers. The permittivity of our system is given as a sum of susceptibilities of the diamond matrix χ_{diam} and the free carriers χ_{FC}:

$$\varepsilon(\omega) = 1 + \chi_{diam}(\omega) + \chi_{FC}(\omega) \tag{3.9}$$

In the absence of free carriers, we can identify $1 + \chi_{diam}(\omega)$ as permittivity of diamond $\varepsilon_{diam}(\omega)$. Then the permittivity of our system is:

$$\varepsilon(\omega) = \varepsilon' + i\varepsilon'' = \varepsilon_{diam} - \frac{\omega_p{}^2}{\omega^2 + \Gamma^2} + i\frac{\omega_p{}^2 \Gamma/\omega}{\omega^2 + \Gamma^2} \tag{3.10}$$

where $\varepsilon'(\varepsilon'')$ is real (imaginary) part of permittivity. Optical manifestation of these relations is given through absorption coefficient α and reflectivity R:

$$\alpha = \frac{\omega\varepsilon''}{cn} = \frac{1}{cn}\frac{\omega_p{}^2 \Gamma}{\omega^2 + \Gamma^2} \qquad R = \frac{(n^2 - 1)^2 + \kappa^2}{(n^2 + 1)^2 + \kappa^2} \tag{3.11}$$

where n is refractive index and κ extinction coefficient:

$$n = \sqrt{\frac{1}{2}\left(\sqrt{\varepsilon'\varepsilon' + \varepsilon''\varepsilon''} + \varepsilon'\right)} \qquad \kappa = \sqrt{\frac{1}{2}\left(\sqrt{\varepsilon'\varepsilon' + \varepsilon''\varepsilon''} - \varepsilon'\right)} \tag{3.12}$$

Relation (3.12) is given through familiar relation $n = \sqrt{\varepsilon_r \mu_r}$ where relative permeability μ_r can be approximated as 1 at optical frequencies.

3.4 Experimental results

We continued our research on the excited carriers in diamond at low temperatures where they undergo phase transition into EHL the details of which were described thoroughly in the previous section. Since the photoluminescence properties were measured quite extensively, we focused on EHL dynamics measured by P&p spectroscopy. There is no inherent absorption in diamond in the IR range, thus the signal detected by this method monitors free-carrier absorption (FCA) described by Drude theory. The extension of the experimental setup to the MIR wavelength was interesting mainly due to testing the limits of Drude theory in describing the EHL because we move beyond the simple FCA. Knowing the density of charge carriers in e-h drops being around 1×10^{20} cm^{-3} (dependent on temperature, see **Fig. 3.2**), the plasma frequency is around ω_{pEHL} = 9.5×10^{14} rad^{-1} which corresponds to the $\lambda_p = 4.7$ μm. Around this wavelength and beyond the response of the system differs compared to the lower wavelength range where the absorption follows λ^2 dependence.

We used a commercially available CVD IIa diamond sample from Element Six. The sample had a very low concentration of impurities, < 1 ppb of boron, and < 5 ppb of nitrogen according to the manufacturer's specifications. The crystal was cut in <100> direction sized 4.5 x 4.5 x 0.5 mm.

Since we were using the MIR probe we measured the absorption in the range of 3 – 10 μm by Fourier spectrometer. The results are in **Fig. 3.3**. This transmission is typical to diamond and given by the sum of Fresnel losses (diamond has a high index of refraction) and absorption on phonons in the 3.5 – 5.5 μm range. Due to the symmetry of the diamond lattice, the one-phonon absorption is forbidden, the absorption in this range is given by two-phonon absorption. Higher multiples of phonons are of course also absorbed, but they are considerably weaker and outside of the MIR range [40].

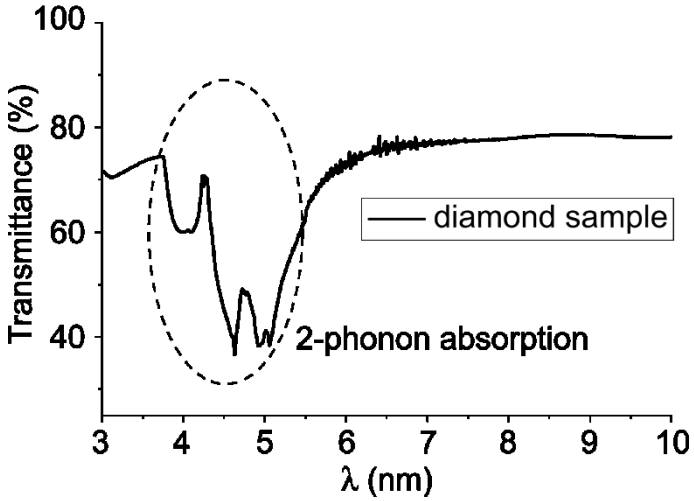

Fig. 3.3 Absorption of our sample in the MIR in the range used in pump & probe measurements measured by Fourier spectrometer.

The high purity of the sample is also confirmed by basic PL measurement seen in **Fig. 3.4** where we can see high-intensity PL of free exciton compared to low-intensity PL in the range of 380 – 600 nm. The band around 400 nm is called "A band" caused by recombination on donor-acceptor pairs, bands around 447 nm and 531 nm are due to dislocations [41]. These two facts show there is a low density of defects, non-radiative and radiative alike.

Zooming on the free-exciton region in **Fig. 3.5** we can see that it consists of several peaks. They are phonon replicas of free-exciton (FE) recombination (diamond being an indirect semiconductor does not manifest no phonon recombination). Decreasing the temperature of the sample two things happen. Firstly the peaks get narrower (higher temperatures lead to Doppler broadening, fitting the exact shape of FE PL can be used to determine the actual temperature of excited carriers). Secondly, the EHL band appears (excitation intensity, I_{exc}, was high). Its spectrum was fitted by equation (3.3) to determine the temperature and density of excited charge carriers inside the liquid which were used later in modeling the response of the system in pump and probe measurements.

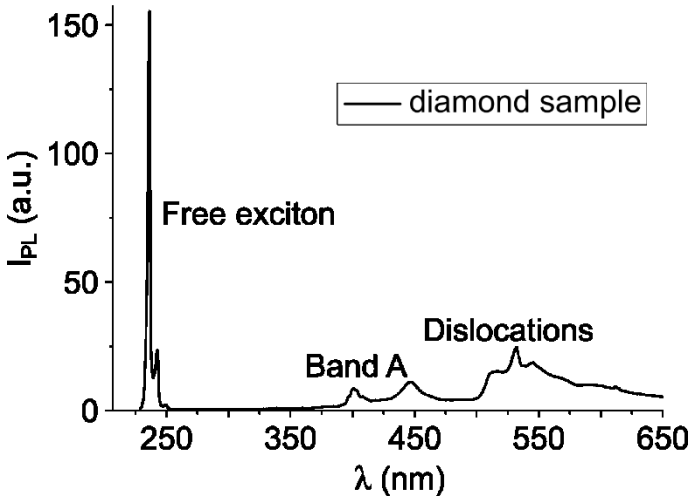

Fig. 3.4 Photoluminescence of the diamond sample excited by a 200 nm laser beam at room temperature.

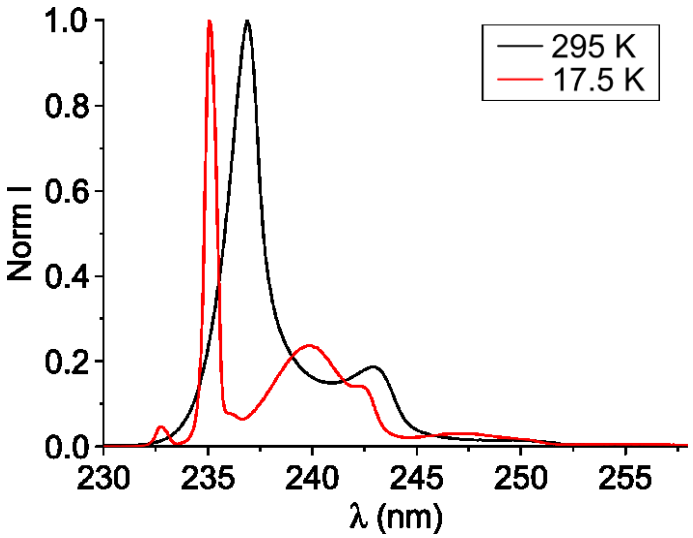

Fig. 3.5 PL of free excitons (295 K) and free excitons with EHL (17.5 K) in diamond sample excited by 200 nm laser beam.

3.5 Dynamics of EHL sensed by MIR probe

We used the measurement system described in chapter 2. The sample was enclosed in a closed-cycle helium cryostat (manufacturer Janis) where the temperature could get as low as 10 K. The widths of the probe and pump beams were chosen to be 90 μm and 300 μm, respectively, to ensure a homogeneous population of excited charge carriers in the probe area.

In **Fig. 3.6** we show the typical signal from pump and probe measurement for temperature below and above T_c. As can be seen, the signals are completely different. The fast decrease of transient transmission is due to the initial creation of an excited carrier population when the pump hits the sample. Then there is a divergence between below and above the critical temperature measurements. Carriers below critical temperature start to condense to EHL. There is an intermediate region circa 10 ps long manifesting as slightly rising, decreasing, or stagnating. In this time range, thermalisation takes place and interferes with EHL condensation. Condensation prevails after 10 ps and the signal reaches its maximum after 50 ps or more (dependent on the initial carrier density).

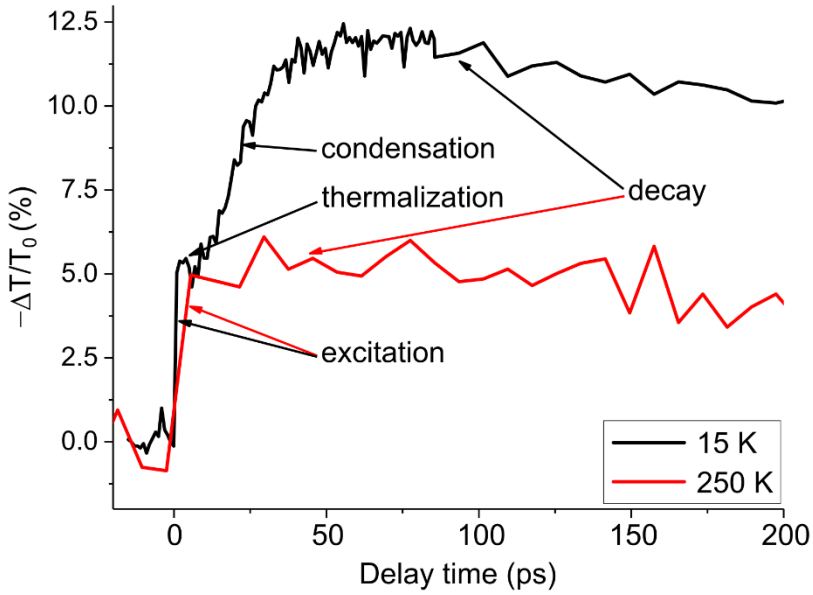

Fig. 3.6 Example of typical P&p signal in diamond excited by 200 nm laser above (red) and below (black) T_c.

Dynamics is influenced by several factors – as is the case for classical liquid there is competition between evaporation and condensation. In our case, there is also recombination meaning that the EHL is a metastable state. In the case of low temperature and high intensity of excitation drops form very rapidly from the nearest excited carriers. In these conditions, drops do not grow large due to the low thermal velocity (after the initial condensation a drop can only grow larger if it joins another drop) and high rate of Auger recombination which causes repulsive phonon wind [42]. Then the recombination becomes dominant.

The dynamics in the above T_c case consists only of the fast rise and decay given by recombination of excitons – we can see that the decay time is well below the radiative time of excitons which is estimated to be between 2 – 3 μs ([43], [44]). The decay time in the one-photon excitation case is determined by fast surface recombination [45]. Even then the decay is roughly twice as long as for EHL where the limit originates from fast Auger recombination given by the high density of charge carriers in drops [46].

It should be noted that the fast rise amplitude is the same for low and high-temperature cases and it is indeed solely given by the initial excited carrier population determined by I_{exc}. Since there are no additional charge carriers generated during the condensation (the average density of carriers stays the same), the changes in transmittance must be due to the higher absorption cross-section of e-h drops. This can be described in the framework of the Drude model by scattering time, τ_s (details were given in the previous section). This is a phenomenological constant with no independent way of determination, even though it must be connected to the local density of excited carriers which is the one parameter changing during EHL condensation.

In **Fig. 3.7** we present the results of the pump and probe measurement with different MIR probe wavelengths for low and high temperatures. The wavelengths are chosen to be below, around, and above λ_p. We tried to stay

away from the regions of increased absorption in the air in our wavelength range (4.1 − 4.8 μm, 5.5 − 8 μm).

Replotting the amplitudes of P&p signal for FE and EHL in **Fig. 3.8**, we can see different dependence of said amplitude on wavelength. Solid curves represent fits by a model described further, dashed curves represent values of absorption coefficient α computed from equation (3.11).

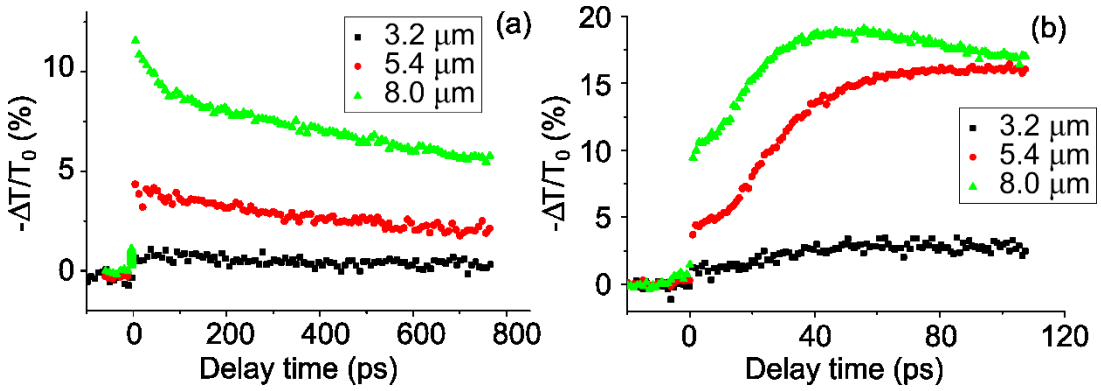

Fig. 3.7 Transient transmission of CVD diamond at 250 K (a) and 13 K (b) for various probe wavelengths. The 200 nm excitation pulse had fluence 0.5 mJ/cm^2.

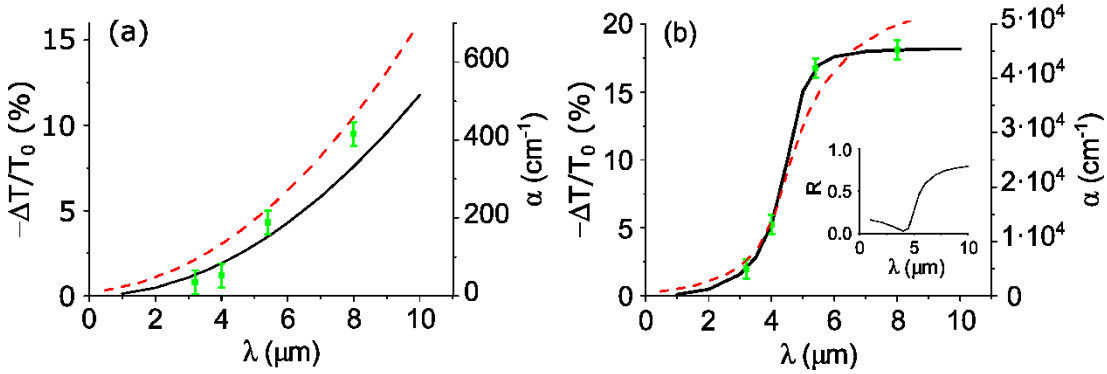

Fig. 3.8 Peak values of the P&p signal in diamond versus the probe wavelength (symbols) for sample temperature 250 K (a) and 13 K (b). Solid curves are the fits by the model described in the text. Dashed curves represent the calculated absorption coefficient α. *Inset:* Dependence of reflectivity of e-h drops on wavelength.

The output of the experiment is given by the difference in transmission values, with general expression for transmission T of the sample with a length l being:

$$T = (1 - R)\exp\left(-\int_0^l \alpha\,(z)dz\right) \tag{3.13}$$

Combining equation (3.13) with equation (3.11) for Drude absorption gives:

$$\begin{aligned} T_{exc}(\omega, \omega_p) &= \left(1 - R_{FC}(\omega, \omega_p)\right) exp\left(-\frac{1}{cn}\frac{\Gamma_{FC}}{(\omega^2 + \Gamma_{FC}^2)}\int_0^l \omega_p^2 dz\right) \\ &= \left(1 - R_{FC}(\omega, \omega_p)\right) exp\left(-\frac{\mathrm{e}^2}{cnm^*\varepsilon_0}\frac{\Gamma_{FC}}{(\omega^2 + \Gamma_{FC}^2)}\int_0^l n_c dz\right) \end{aligned} \tag{3.14}$$

where subscript FC denotes quantities corresponding to the free charge carriers generated by excitation and R_{FC} is reflectivity generated by surface excited charge carrier density.

Integral in equation (3.14) results in the total number of excited charge carriers on the unit area in the probe beam path. The final formula for T_{exc} is then:

$$\begin{aligned} T_{exc}(\omega, \omega_p) = &\left(1 - R_{FC}(\omega, \omega_p)\right) \\ &\times exp\left(-\frac{\mathrm{e}^2}{cnm^*\varepsilon_0}\frac{\Gamma_{FC}}{(\omega^2 + \Gamma_{FC}^2)} I_{ph}(1 - e^{-\alpha_{200}l})\right) \end{aligned} \tag{3.15}$$

where α_{200} is the absorption coefficient of diamond at the wavelength of 200 nm and I_{ph} is the density of pump photons in the area of the probe beam S_{probe}. This quantity is computed as follows:

$$I_{ph} = 2\frac{N_{ph}}{S_{probe}\pi w_{pump}^2}\int_0^{w_{probe}}\int_0^{2\pi} r \cdot exp\left(-\frac{2r^2}{w_{pump}^2}\right)dr = \frac{N_{ph}}{\pi w_{probe}^2}\left(1 - exp\left(-\frac{2w_{probe}^2}{w_{pump}^2}\right)\right) \quad (3.16)$$

where N_{ph} is the number of photons in one laser pulse and w_{probe} (w_{pump}) the Gaussian radius of probe (pump) beam. Technically the scattering frequency Γ_{FC} is dependent on the excited charge carriers density which depends exponentially on the *z*-axis in the case of one-photon excitation. But as was noted above, it is a phenomenological constant and fitting parameter at that. The resulting value is thus just an averaged value across the excitation depth.

Equation (3.15) inserted into $\Delta T/T_0 = (T_{exc} - T_0)/T_0$ models the experimental values in high-temperature case fairly well. The only fitting variable is $\Gamma_{FC,}$ all other parameters were determined independently. A slight discrepancy at 8 μm will be addressed later but looking at dynamics, it can be seen that it behaves quite differently than lower wavelengths. Best fit gives a value for $\Gamma_{FC} = 4.9\times10^{13}$ s^{-1} (in terms of scattering time τ_s = 20 fs). As can be seen in **Fig. 3.8a**, the dependence of the ΔT signal tracks with the dependence of absorption coefficient.

For the low-temperature case, this dependence looks different. This can of course be just due to the difference in plasma frequency of the system – absorption does not follow a simple λ^2 dependence which is present well above plasma frequency (as is the case for high-temperature measurements). Comparing the dashed curve in **Fig. 3.8b** to the solid one, we can see that it does not track as in **Fig. 3.8a**. There is a flat region of the signal from ~6 μm onward, but absorption itself has this region around 11 μm. Therefore there must be another parameter that influences the signal significantly. The only other parameter in equation (3.13) is reflectance. In the inset in **Fig. 3.8b** we plot reflectance depending on wavelength. It rises strongly when we get below plasma frequency and flattens in the wavelength range of our interest.

To use the same approach to model the wavelength dependence of our signal, we must make a few changes because the situation is quite different in the case of EHL. We move from a homogeneous system of excited carriers to an inhomogeneous system where we have high-density drops and low-density exciton gas.

For the condensation to be possible, the smallest density of carriers $n_{tresh} = 10^{15}$ cm^{-3} [38]. This means that EHL will be present only up to a certain depth d computed as $1/\alpha_{200} \times \ln(\alpha N_{ph}/n_{tresh})$ that in our case is 18 μm. We assume that up to this depth all excited charge carriers condense into EHL; the rest of the excited volume keeps the low-density character, i.e. the electrons and holes stay as excitons. We depict the situation right after the excitation in **Fig. 3.9**. The red rectangle shows the area monitored by the probe beam where the condensation occurs (in reality it is a cylinder with a base given by the probe beam profile and height equal to d).

To allow a computation with equation (3.13) we rearrange the system in such a way that we have two continuous areas – an inner cylinder consisting of EHL and an outside that has no excited carriers. Since we must maintain the

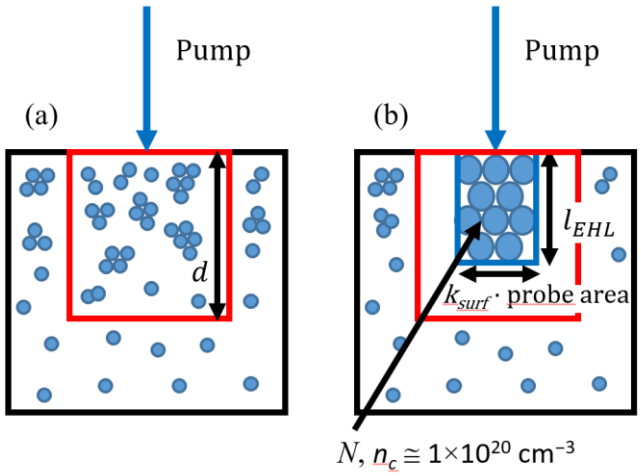

Fig. 3.9 (a) Situation in the sample after the condensation. We monitor the arrangement of charge carriers in EHL in the red rectangle. (b) The simplest computational rearrangement of the situation (a).

same total number of excited charge carriers, the volume of the EHL cylinder compared to the excited volume must shrink according to the ratio of excited charge carrier densities, i.e. the volume of EHL will be smaller by a factor of n_{EHL}: n_c. We know from PL that n_{EHL} in our case was 1.1×10^{20} cm^{-3}, the averaged density n_c is 5.2×10^{17}cm^{-3}. We expect the most e-h drops to be near the surface where most of the excited charge carriers are, but the exact arrangement is unknown. Since EHL interacts with light through absorption (its contribution is given by the height of the cylinder) and reflection (its contribution is given by the base of the cylinder), we can estimate a crude arrangement of EHL from the resulting fit parameters.

Defining k_{surf} as a portion of probe photons passing through EHL, it is simply given by the ratio of cylinder base S_{EHL} in our new arrangement to the probe beam area S_{probe}. The height of the cylinder l_{EHL} effectively represents the average number of drops the probe photons encounter passing through EHL. We will consider l_{EHL} an independent fitting parameter through which we can determine k_{surf} as follows:

$$k_{surf} = \frac{S_{EHL}}{S_{probe}} = \frac{N_c}{l_{EHL} n_{EHL} S_{probe}} \tag{3.17}$$

where $N_c = I_{ph}(1 - e^{-\alpha_{200} d}) = S_{EHL} l_{EHL} n_{EHL}$ is the total number of excited carriers that undergo condensation.

Due to the constant carrier density in EHL, the integration in equation (3.14) is trivial and the resulting T_{exc} is:

$$\begin{aligned} T_{exc}(\lambda) = {} & k_{surf}\big(1 - R_{EHL}(\lambda)\big) \exp(-\alpha_{EHL}(\lambda) l_{EHL}) \\ & + \big(1 - k_{surf}\big) T_0 \end{aligned} \tag{3.18}$$

where the first term represents probe photons encountering EHL and the second term photons which pass undisturbed - we neglect the rest of the sample from *d*

onwards because its influence due to the low excited charge carrier density is negligible.

Inserting (3.17) and (3.18) into $\Delta T/T_0$ gives us the final relation:

$$\frac{\Delta T(\lambda)}{T_0} = \frac{N_c}{T_0 S_{probe} l_{EHL} n_{cEHL}} \times \times \left(\left(1 - R_{EHL}(\lambda)\right) \exp(-\alpha_{EHL}(\lambda) l_{EHL}) - T_0 \right) \tag{3.19}$$

The resulting value of scattering rate is Γ_{EHL}= 8.2×10^{13} s^{-1} with the corresponding scattering time τ_{sEHL} = 12 fs. The value of l_{EHL} is 0.48 μm. According to [47] the e-h drops in our conditions (low temperature, high excitation intensity) contain on average only 2-3 e-h pairs; that makes them only ∼4 nm large. Thus each probe photon effectively interacts with ∼120 e-h drops on average.

As can be seen, the model fits the results very well. We neglect the effect of Rayleigh scattering which should be minimal – the size of the drops is 3 orders smaller than our probe beam wavelength. The resulting values of scattering times for EHL and FC are two times smaller than previously published in [48], but interestingly their ratio is very similar. The discrepancy can partly be due to different sets of electron and hole masses being used, the current set of masses was not known at the time of [48] publication.

3.6 Quantum model of free carrier absorption

As we noted previously there is a discrepancy in modeling the response of 8 μm photons on free carriers at higher temperatures. Namely the one exponential decay changes to two-exponential with the additional component being much faster. Signal depending on I_{exc} is in **Fig. 3.10a**. We can see that the lowest I_{exc} does not seem to exhibit the two-exponential behavior but normalizing the results in **Fig. 3.10b** we can see why. The noise of the

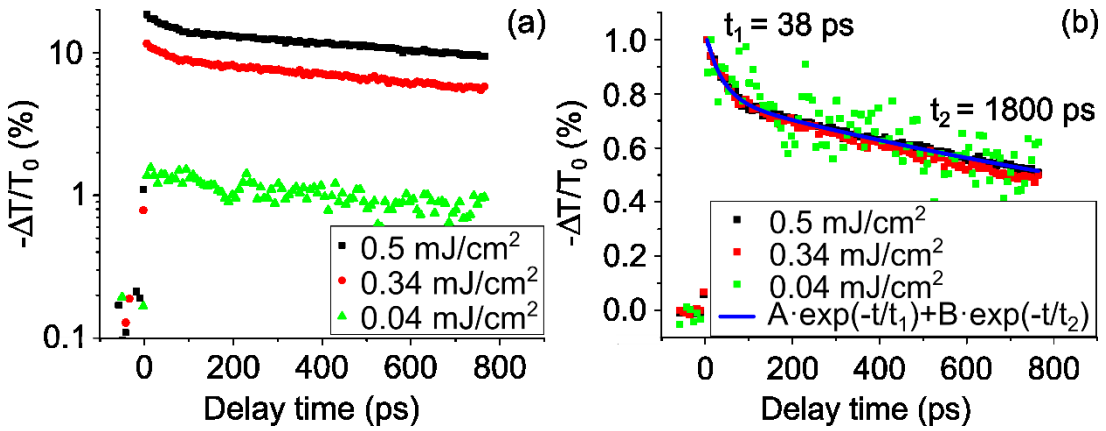

Fig. 3.10 (a) Transient transmission at 250 K for 8 μm at different excitation fluences (excited carrier densities 4.4×10^{18} – 3.5×10^{17} cm^{-3}) (b) Normalized transient transmission along with two-exponential decay fit (line).

measurement is too high to discern the 2nd decay component. But for the other I_{exc}, the 2 components keep their amplitude ratio 1:4 (fast:slow) and the fast decay stays the same. The slow component is slightly longer for higher I_{exc} as was expected. The prolongation of exciton lifetime in the case of one-photon excitation observed in [49] was explained as carrier-carrier scattering slowing the diffusion to surface, which is the main recombination channel in this type of excitation. The decay time of the long component, 1800 ps is in line with previous measurements.

The short component can hardly be explained in the framework of the classical Drude model since it monitors only the excited carriers density. If there was such two-component decay in density, we would see it in all probe wavelengths. Its decay time is on the order of excited carrier relaxation times in diamond [50], so we have looked at how this mechanism can be incorporated into our description. One way is the quantum mechanical theory of the free-carrier absorption which takes into account the carrier relaxation and scattering on acoustic and optical phonons [51]. It is basically an intraband transition where photon interacts with the free carrier through matrix element $|H_{kk'}|$, where k is the initial momentum of the carrier which is given by its position in the band, and k' is the final momentum of the carrier, i.e. the final position in

the band. These positions are connected by phonon with momentum q, $k' = k \pm q$.

To simplify the calculation of the integral $|H_{kk'}|$ we consider the bands to be parabolic and the excited charge carriers to be in quasi-equilibrium – their distribution in the band can be described by Boltzmann distribution with effective temperature T_e. These conditions are valid close to the bottom of the bands and at times after carrier-carrier relaxation takes place which usually takes a few fs.

In this framework the absorption coefficient consists of four contributions, each representing an interaction where photon or phonon are either emitted or absorbed:

$$\alpha = \alpha_a^+ + \alpha_a^- - \alpha_e^+ - \alpha_e^- \tag{3.20}$$

where the lower index signifies photon absorption (a) or emission (e) and upper index *phonon* absorption (+) or emission (-).

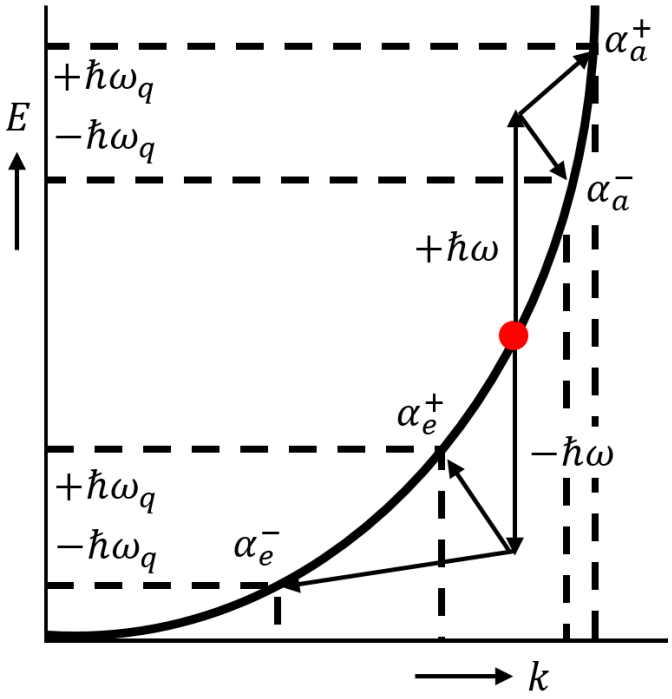

Fig. 3.11 Depiction of different interactions of a charge carrier (red circle) with a photon and a phonon with frequencies ω and ω_q, respectively.

These contributions are depicted in **Fig. 3.11**. The individual absorption coefficients are computed as follows [52]:

$$\alpha_a^{\pm} = \frac{\mu_0 c}{\sqrt{\varepsilon}} \frac{2^{\frac{3}{2}} n_c e^2 m^{*\frac{1}{2}}}{3\pi^{\frac{3}{2}}\hbar^5\omega^3} (k_B T_e)^{\frac{3}{2}} V \times \\ \times \int_0^{\infty} |H_{kk'}|_{\mp}^2 \, exp(z_{\mp}) exp\left(-\frac{1}{2}\left(\xi + \frac{z_{\mp}^2}{\xi}\right)\right) \xi d\xi \tag{3.21}$$

where μ_0 is vacuum permeability, V volume, and the ξ and z± are:

$$\xi = \frac{\hbar^2 q^2}{4m^* k_B T_e} \qquad\qquad z_{\pm} = \frac{\hbar\omega \pm \hbar\omega_q}{2k_B T_e} \tag{3.22}$$

where ω_q is phonon wavelength.

For photon emission the only thing that changes in equation (3.21) is that the $z_{\pm}$ have $-\hbar\omega$ in the numerator.

Symmetry introduced through parabolic band approximation causes scattering to occur only on longitudinal acoustic and transverse optical phonons [53]. To further simplify the calculation we can neglect the dispersion relations for optical phonons and replace them with a constant $\hbar\omega_q$ = 165 meV. For acoustic phonon, we can approximate dispersion relations with a linear dependence $\omega_q = \nu_l q$ where ν_l is the longitudinal velocity of sound in diamond with the value of 17.5 km/s [54].

The matrix elements for scattering on optical and acoustic phonons, $\left|H_{k\pm q,k}\right|_{opt}$ and $\left|H_{k\pm q,k}\right|_{ac}$, respectively, differ from each other only in their dependence on phonon momentum q:

$$\left|H_{k\pm q,k}\right|_{ac} = \epsilon_{ac} q \sqrt{\frac{\hbar\left(N_q + \frac{1}{2} \mp \frac{1}{2}\right)}{2\varrho V \omega_q}} \tag{3.23}$$

$$\left|H_{k\pm q,k}\right|_{opt} = D\sqrt{\frac{\hbar\left(N_q + 1/2 \mp 1/2\right)}{2\varrho V \omega_q}}$$

where D and ϵ_{ac} are deformation potential constants and N_q is the average number of phonons at a temperature T given by Bose-Einstein distribution:

$$N_q = \left(exp\left(\hbar\omega_q/k_B T\right) - 1\right)^{-1} \tag{3.24}$$

We can see that the free carrier absorption is sensitive to the phonon population. Our excitation of 200 nm produces excited charge carriers with ~0.7 eV excess energy. This excess energy raises the effective temperature of carriers and also produces phonons during thermalisation. High I_{exc} thus influences the fast component in two ways – higher excited carrier density and higher phonon population. It is then understandable that the fast component is unobservable for low I_{exc}.

Integral in equation (3.21) (and its counterpart for emission) has an analytic solution for optical phonons due to our approximation but must be solved numerically for acoustic phonons. The resulting absorption coefficients for interaction with acoustic (solid lines) and optical (dashed lines) phonons are plotted in **Fig. 3.12** depending on the photon wavelength and in **Fig. 3.13** based on the effective temperature. The values of deformation potentials were taken from [55] to be ε_{ac} = 12 eV and $D = 4\times10^8$ eV/cm.

The computation shows that scattering on acoustic phonons is much stronger than scattering on optical phonons. This was already established in ([56], [57]) and our data support this result further since we found no trace of optical phonon resonance. Due to the high energy of optical phonons in diamond this resonance should be measurable even at moderate temperatures and not only at low temperatures as is common. Also, optical phonons decay very fast (in ~10 ps [58]) into two acoustic phonons with half energy each further enhancing acoustic phonon scattering. Lastly, if the scattering on optical

phonons was dominant then we would see the fast component also for the probe wavelength 5.4 μm. Looking at **Fig. 3.13** we can see that for effective temperatures up to 500 K optical phonon scattering for this wavelength is comparable to 8 μm.

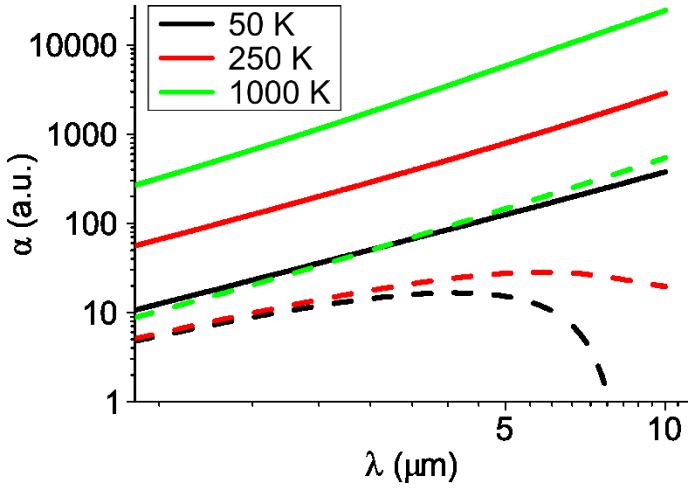

Fig. 3.12 Dependence of absorption due to the scattering on acoustic (solid lines) and optical (dashed lines) phonons on wavelength for various effective carrier temperatures T_e. The temperature of diamond matrix T = 250 K.

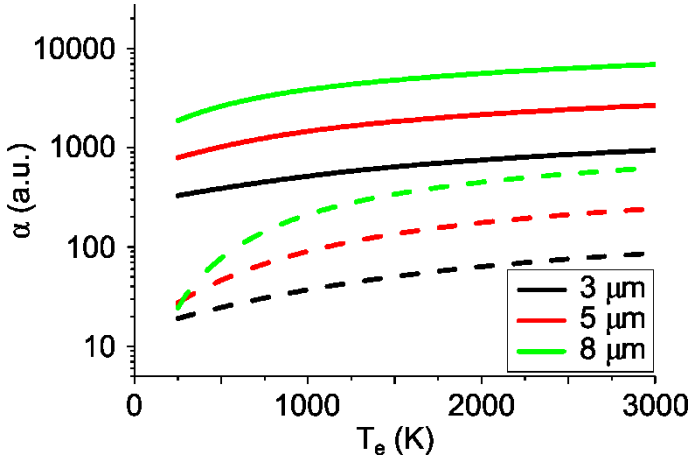

Fig. 3.13 Dependence of absorption due to the scattering on acoustic (solid lines) and optical (dashed lines) phonons on carrier temperature for several photon wavelengths. The temperature of diamond matrix T = 250 K.

Zooming on the temperature dependence of the absorption coefficient there is a higher slope of this dependence for longer photon wavelengths. That means the longer probe wavelengths are more sensitive to changes in the effective carrier temperature. Let us define the first derivative of α as a function of T_e as η. In **Fig. 3.14** we compare these derivatives for probe wavelengths 5 and 8 μm. As can be seen from their ratio, 8 μm is essentially 3x more sensitive to the effective temperature change up to 1000 K. This explains why we did not see any fast component for this probe wavelength (**Fig. 3.7**) even though the overall level of the signal was not low.

What we monitor with the 8 μm probe is the carrier relaxation by acoustic phonons which takes place after the fast relaxation by optical phonons. Excited carriers shed their excess energy in the first hundreds of fs mostly through optical phonons [50]. They then reach a point where their excess energy is below the energy of one optical phonon. That is ≈140 meV which roughly translates to the effective temperature of 530 K (using $T_e = E_{exc}/3k_B$). Then the relaxation through acoustic phonons takes place on the timescale of tens of ps.

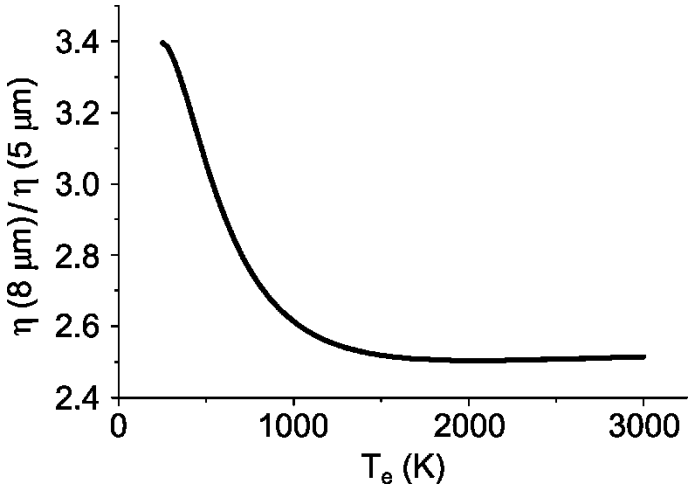

Fig. 3.14 Temperature dependence of η (8 μm)/η (5 μm) to the excited charge carriers temperature for the case of scattering on acoustic phonons.

Conclusion

In this chapter, we showed the benefits of using MIR probe beams supplied by our home-built system in measurements of transient transmission. We investigated the photoexcited electron-hole system above and below its plasma frequency and were able to validate the usefulness of the Drude theory in describing such a system even around critical points. We showed that the measurements in this wavelength range can help estimate the arrangement of e-h drops in the excited region.

We also found that the transient transmission dynamics for a long-wavelength probe pulse exhibit an additional faster component which we interpreted in terms of carrier thermalisation. We had to move beyond the Drude theory to the quantum model of free carrier absorption which also revealed two significant facts: 1) the induced absorption is mainly due to the scattering on acoustic phonons and 2) the wavelength dependence predicted is very similar to the classical theory. This explains why we were able to use Drude theory in predicting the system response successfully when we were not concerned about excited carrier dynamics.

The higher sensitivity of long probe wavelengths to the change of the light absorption coefficient with the effective carrier temperature allowed us to monitor the thermalisation of high-density charge carriers.

4 Silicon nanocrystals in SiO_2 matrix

In this chapter, we will present our results from the measurement of luminescence of silicon nanocrystals embedded in the SiO_2 matrix. We wanted to study if introducing dopants (boron, phosphorus) during sample fabrication would lead to the generation of free electrons or holes as is in the bulk case. According to that interest, the samples were prepared externally in IMTEK at the University of Freiburg. We will start with a general overlook of silicon and its impact on the industry. Then we will describe the transition to nanocrystals, their effects, and potential applications. These will be followed by a description of our samples, experiments, and discoveries. The results in this chapter were published in [59].

4.1 Silicon

Silicon has been the main material in electronics since the discovery of the transistor in 1947. Many decades of its use refined its technology close to perfection. This overcomes many disadvantageous electronic properties this material has and places all new materials on the back foot (previously mentioned diamond is such a material, technology of which is still comparatively nascent). Also, the natural abundance of silicon is too a major advantage. Hence much effort has been made to overcome the disadvantages of silicon by advanced fabrication to benefit from established technology.

One such disadvantage is that silicon is poor optical material. Due to the indirect bandgap, the probability of interaction with photons is rather low. But since the purity of the fabricated material can be made almost absolute, silicon is widely used as a detector or photovoltaic cell. For many applications, it would be advantageous to have silicon where the electron-photon interaction is enhanced. This can be achieved by making nanocrystalline silicon where some

conditions limiting the effectiveness of such interaction are relaxed. Of many varieties of silicon nanostructure, we will focus on the so-called quantum dots which are structures where every dimension is limited to tens of nanometers. From here on we will use nanocrystals instead of quantum dots.

4.2 Silicon nanocrystals

First silicon nanocrystals (SiNCs) were synthesized in the early 1990s ([60], [61]) already with two different techniques. These early experiments already led to visible PL from silicon which in its bulk form has PL at 1137 nm (1.09 eV) with quantum efficiency 5×10^{-7} and decay time of 560 ms [62]. Comparatively, the first SiNCs had a quantum efficiency of 3% and decay time of 70 μs [63].

The techniques of fabrication branched and progressed significantly, the SiNCs can be fabricated by pulsed laser ablation ([64], [65]), ball milling [66], from sol-gel precursors ([67], [68]), from plasma [69], by ion implantation [70] in form of superlattices [71], etc.

The used technique leads to different distributions of sizes, passivation/surface modifications, crystallinity, and character of PL. PL can be generally differentiated into a red/infrared S-band (S due to slow decay in tens to hundreds of μs) and a blue F-band which decays in tens of ns. SiNCs can possess both the S- and F-band or just one of the two. Due to the above-mentioned factors analyzing the PL is quite complex. The origin of the S-band seems to be well established being from band-to-band recombination. The origin of the F-band is still controversial and probably the origin differs on a case-to-case basis ([72], [73]). Indeed, in recent years the origin of the F-band in nanocrystals that do not exhibit the S-band came into question ([74], [75]).

Apart from the size of nanocrystals, the surface has a paramount influence on PL character. The smaller the NCs the higher percentage of atoms

are located on the surface compared to the core. The “purest” type of surface passivation is hydrogen since it has a very small influence on core atoms which makes it a perfect model system for the theory of SiNCs. Sadly, this type of surface is unstable in the ambient atmosphere and especially under UV excitation [76]. Hydrogen is substituted by oxygen which introduces defects (e.g. dangling bonds) and in-gap states for the smallest of NCs (< 2 nm [77]) limiting the PL tunability of NCs. But surface can be passivated by many other agents ([78], [79], [80], [81]) which are resilient to oxidation (in the case of long alkyl chains the passivation is not perfect since bound alkyls block some open Si sites for other alkyls). Actually, the core and surface are not cleanly separated in nanocrystals since the “core” wavefunction due to uncertainty relations extends to the surface [82] and a high percentage of Si atoms are actually at the surface. The type of surface determines the ability of SiNC to manifest effective PL, the position of the PL band (PL can be shifted due to strain [83] or electric field [82] generated by surface groups), and the quantum yield. The character of luminescence of a particular NC can be also completely switched by surface modification [84].

The crystallinity of nanocrystals is another parameter that determines if they are optically active or not. Since the nanocrystals contain only a few hundred to several thousand silicon atoms, there are not many lattice repetitions in the smallest ones. Core atoms should be in crystal lattice but how far this “zone” extends is not so easily determined. It seems that the influence of the ordered structure is greatly diminished for the smallest nanocrystals (over 90% of atoms of 3 nm NC constitute of surface layer [85]). This induces strain-producing defects in the structure which leads to an effective size of the ordered core of just around 1.2 nm (around 3 unit cell lengths) [86].

As can be seen the energy structure of silicon experiences many different modifications when going from bulk to nanosize. The bandstructure of bulk silicon is in **Fig. 4.1**.

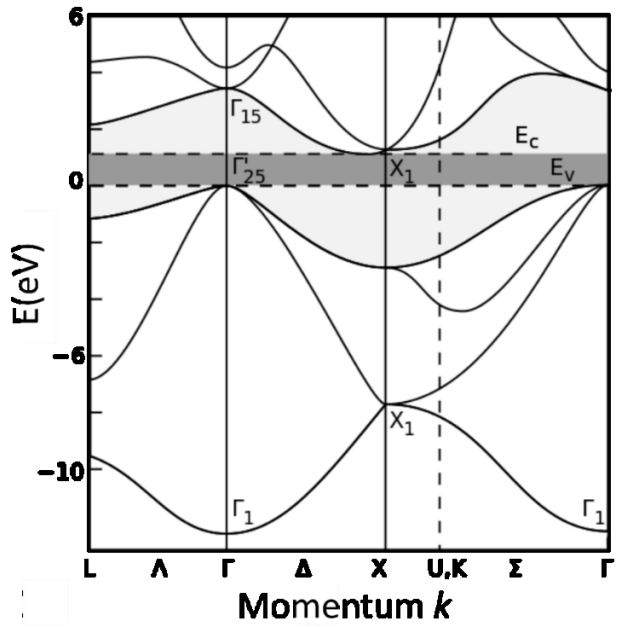

Fig. 4.1 Band structure of silicon [87]. The indirect bandgap is between Γ_{25} point and the lowest point of the X_1 valley.

When we decrease the dimensions of the crystal lattice to the size comparable to Bohr radius of the exciton (5 nm in silicon), the so-called quantum confinement effect results in the discretization of energy bands and also the indirect bandgap shift to higher energies, i.e. the smaller the nanocrystals the higher its emission energy. From effective mass theory approximation, the energy shift of PL peak on nanocrystal size R can be described as follows:

$$E_{PL}(eV) = E_g(eV) + C/R^2 \tag{4.1}$$

where E_g is the indirect bandgap energy of bulk and C is the confinement parameter. C is predicted to be between 7–14 depending on the computational model used [88].

This description is valid only for the idealized case of a perfect 1D crystal. In the case of real nanocrystals, it can serve only as a crude approximation. Firstly, for very small SiNCs it is hard to describe them as crystals since the periodicity is limited to a few lattice constants. The dependence can follow a general power law (i.e. $1/R^x$ where x is not necessarily

2) ([89], [90]). Real energy level distribution is very complex [91] and heavily depends on the surface groups or shape of the surface.

Another effect of the nanostructure is the real-space localization of excitons. Due to the Heisenberg uncertainty relations real-space localization results in delocalization in *k*-space. Thus the overlap of electron and hole wavefunctions is larger and firstly, there is a higher probability of recombination and secondly, there can also be quasi direct transitions ([92], [93]), i.e. transitions without phonon. These effects lead to the shortening of radiative decay times for small nanocrystals (to ns range) and can result in internal quantum yield close to 1 ([94], [95]). Also, the behavior of the direct bandgap is different compared to the indirect gap – it actually narrows for smaller nanocrystals (due to different band curvature at Γ_{15} point [96]).

There are many potential applications for SiNCs, e.g in photovoltaics to overcome the Shockley-Queisser limit ([97], [98]), as tiny light sources integrable on silicon chips [99], as fluorescence markers in biological/medical research ([100], [101]) (SiNCs were found non-toxic in cells [102], [103]), as anode material in Li-ion batteries [104] etc.

SiNCs can also be used in hybrid materials in which they are mixed with or directly bonded to different species in which they can serve a double role. Either as an energy collector (energy is transferred from extrinsic material to the NC) or an emitter (energy is transferred out of the NC). As an example of the first case, molecules with high absorption outside of the SiNC absorption band ([105], [106]) were used. For the latter case, high absorption of SiNCs in the UV region can be exploited for excitation of Er^{3+} ions in silica [107] or as a multi-chromatic emitter [108].

4.3 Preparation of SiNC samples

The samples were developed and prepared by a superlattice approach in the group of M. Zacharias. This method produces very well controlled

nanocrystalline parameters like density, size, and passivation. Originally [71], it was based on the deposition of alternating layers of SiO_2 and SiO_x (also called silicon-rich oxide layer) where *x* is around *1*. After the deposition, this sample is annealed at 1100 °C for 1 h under N_2 atmosphere. During the annealing, the phase separation occurs in the SiO_x layers described by:

$$SiO_x \rightarrow \frac{x}{2} SiO_2 + \left(1 - \frac{x}{2}\right) Si$$

As can be seen, the parameter *x* controls the density of emerging nanocrystals. The size of nanocrystals is independently controlled by the thickness of the SiO_x layer.

This "recipe" produces SiNCs in silicon-rich oxide (SRO) layer where the deposition happens from O_2 and SiH_4 diluted by high purity Ar precursor gases. An alternative was developed [48] where O_2 is replaced by N_2O producing silicon-rich oxynitride layer (SRON) SiO_xN_y. N_2O gas has the advantage of being safe (compared to explosive O_2) and also offers reliable control of *x* in the interval $0 \leq x \leq 2$. This in turn enables precise control of NC density-independent of the layer thickness. A different matrix has no adverse effects on PL, only the annealing process is slightly changed to accommodate for a slower crystallization rate due to the lower mobility of Si in nitrogen-containing oxides.

To passivate defects on the boundaries between nanocrystals and the matrix, samples can be treated to the second annealing at 450 °C in an atmosphere of 5% H_2 in N_2 for 1h [109], which enhances PL intensity by one order of magnitude [110]. Another possibility to increase the PL efficiency is to have sufficiently thick SiO_2 layers between the NC layers, at least 2 nm [111]. This weakens thermally activated transport of excitation into non-radiative centers.

These two recipes each offer a different possibility of adding Si dopants. Electronics being based on PN junction requires successful doping to create

p type and n-type materials. Successful meaning that the incorporation of dopants results in the creation of free carriers at the operating temperature of the PN junction. In our case boron (B) was used for p-type doping and phosphorus (P) for n-type one. Due to technical reasons, the process based on SiO_xN_y layers enabled good control of phosphorus incorporation, whereas the process based on SiO_x layers was used for incorporation of boron.

Concretely our first sample set is described in **Table 4.1**. Each sample is made up of 50 bilayers of SiO_2/SiNCs deposited on the n-type (100)-Si substrates. The areal density of SiNCs is around 2.4×10^{12} cm^{-2}. Samples can be divided broadly into two sets – SRON and SRO – each set contains a combination of passivated (designated by –H suffix) and "doped" (designated by –P and –B suffixes, respectively) samples. The thickness of SiO_2 layers is 4 nm each, the thickness of the NC layer is 4.5 nm.

Due to the reasons described later, we used also a second sample set which included smaller nanocrystals (and thus narrower SiNC layer), a reference monolayer of pure SiO_2, and one with boron. Samples with smaller nanocrystals are designated with -# suffix where # is the diameter of NCs. Their list is in **Table 4.2**.

An illustrative image of our samples and their fabrication is in **Fig. 4.2**.

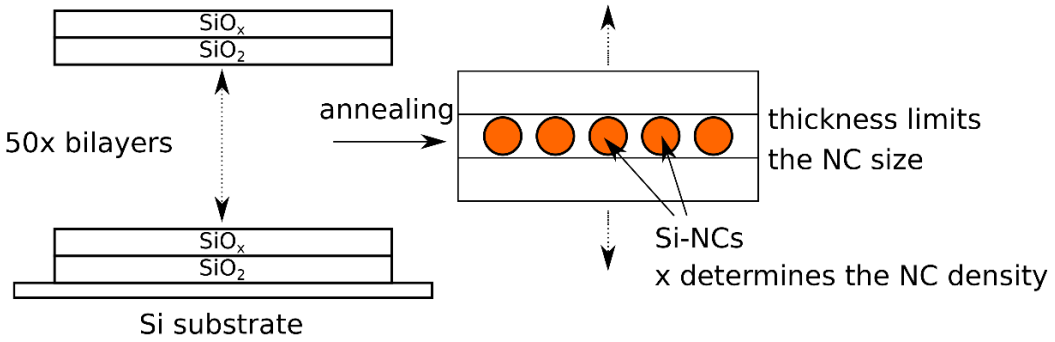

Fig. 4.2 Schematic representation of the fabrication of our samples.

Sample	NC size	Dopant	Pass.	Sample	NC size	Dopant	Pass.
SRON	4.5 nm	None	Yes	SRO	4.5 nm	None	Yes
SRON-H_2	4.5 nm	None	Yes	SRO-H_2	4.5 nm	None	Yes
SRON-P	4.5 nm	P	None	SRO-B	4.5 nm	B	None
SRON-P-H_2	4.5 nm	P	None	SRO-B-H_2	4.5 nm	B	None

Table 4.1 Sample set 1 – All the sample designations with important characteristics. As noted in the text all the samples consist of 50 bilayers deposited on the n-type Si-substrate by PECVD. This sample set focuses on the comparison of the influence of doping/passivation on the PL.

Sample	NC size	Dopant	Pass	Sample	NC size	Dopant	Pass
SRO-3-B-H_2	3 nm	B	Yes	Ref	None	None	None
SRO-4-B-H_2	4 nm	B	Yes	Ref-B	None	B	None
SRO-5-B-H_2	5 nm	B	Yes				

Table 4.2 Sample set 2 – All the samples designations with important characteristics. All samples were made the same way as the ones in **Table 4.1** apart from references Ref(-B) which consist of 300 nm SiO_2 monolayer deposited on the same substrate as SiNC samples. This sample set focuses on the influence of size on the PL.

4.4 Experimental results

The principal method of our investigation was TRPL using a streak camera (described in Chapter 1) with a maximal time resolution of 15 ps. If the free electrons or holes were present in the "doped" samples, we would expect a higher rate of Auger recombination compared to the "undoped" samples since the always present free carrier would interact with the temporary excited carrier.

We started with the first sample set. Before the time-resolved measurements, we did some basic characterization of PL by continuous-wave (CW) excitation with HeCd laser. The results for the first sample set are in **Fig. 4.3**. Even though the thickness of NC layers is similar, the PL max of both types of samples (SRO, SRON) is quite different; for SRO the max is in the range of 825 – 875 nm, for SRON the range is 925 – 960 nm. PL of NCs depends not only on their size but also on their surroundings [112]. The matrices are not the same which probably leads to such a PL shift. There are also minor PL shifts in between the samples of a single type.

Firstly, the H_2-passivation redshifts PL. This is due to the larger NCs having a higher chance of containing defects [113]. Due to the spread of the wavefunction, a single defect quenches PL.

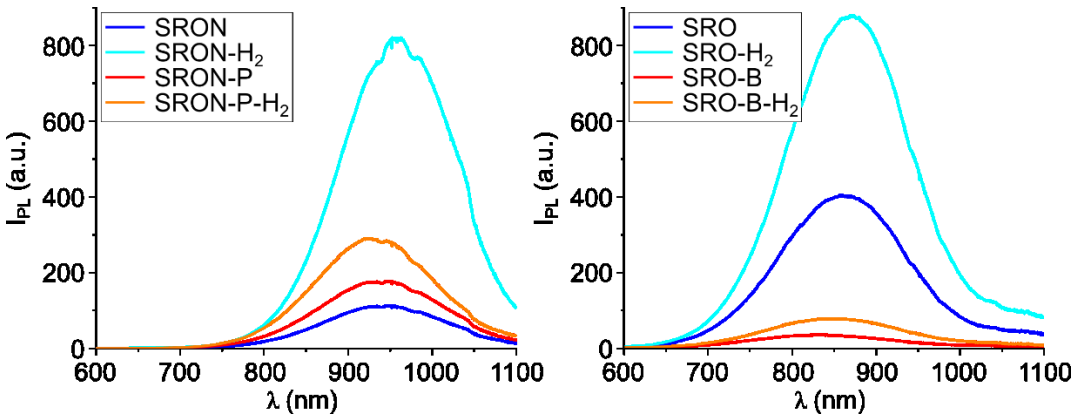

Fig. 4.3 PL spectra of the first sample set (**Table 4.1**). Samples were excited by continuous HeCd laser, 325 nm, measured PL is thus time-integrated.

When the defects are passivated, the larger NCs dominate PL because they have larger absorption cross-sections [114]. On the other hand samples with dopants have blueshifted PL. This shift is attributed to a change of excess Si content during fabrication ([115], [116]). The PL intensity also increases after phosphorus has been added (phosphorus passivates some defects [116]) and decreases with boron doping (boron only introduces more defects [115]).

We excited those samples by the 3rd harmonics of PHAROS laser, 343 nm (3.61 eV), and looked at the differences in the PL decays between the samples (**Fig. 4.4**). The supposedly increased Auger recombination rate would manifest as a sharp decrease at the beginning of PL decay of "doped" samples. Looking at the results of the SRON samples, we can see that the only sample showing a sharper initial decrease is the one without any treatment, which is also in line with CW excitation results discussed above where the pure SRON sample showed the lowest PL efficiency. Clearly, no free carriers were created as a result of P incorporation and that initial decrease can be attributed to defects. In the case of SRO samples, B incorporation *shows* an initial decrease in PL decay, but not on the expected time scale. Still, there is another effect influencing PL, which is not explainable just as an increased presence of defects since it is present also in the sample treated with H_2 passivation. Before we proceed to this part of our investigation, let us briefly mention the results by our colleagues running concurrent experiments leading to the same conclusion that no free carriers are created through B or P incorporation.

A series of samples with increasing concentrations of boron or phosphorus were fabricated to investigate their influence on PL [117]. For reasonable concentrations of these "dopants" up until one such atom can be expected in *every* nanocrystal, the PL does not decrease significantly and its peak does not shift – with increasing concentration of B or P, the whole PL spectra should blueshift since bigger (thus redder in PL) NC are expected to have a higher probability of incorporating these atoms. The effect of doping can also be "deactivated" by cooling the samples since the external charge carriers

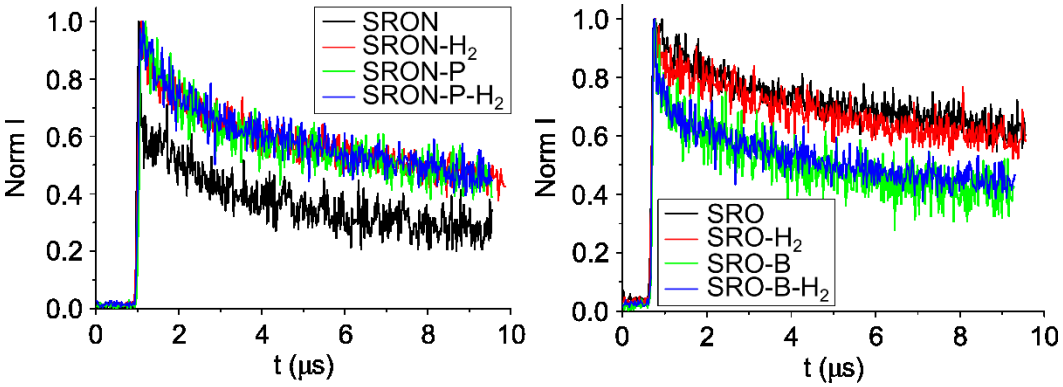

Fig. 4.4 Normalized PL decays of the sample set 1 for I_{exc} = 6 mJ/cm^2 in the 10 μs time window.

need to be thermally ionized into the conduction or valence band. Decreasing the sample temperature should thus lead to the redshift in PL. But a slight blueshift was actually observed which was attributed to the thermal contraction of the lattice. Lastly, the transient transmission measurement did not show any significant differences between the signals from doped and reference samples.

We continued our study by varying I_{exc} from 0.2 to 100 mJ/cm^2. The spectra integrated over the first 100 ms (90% of the longest part of PL is radiated in this window) after excitation are in **Fig. 4.5**. As can be seen in our spectral detection window we monitored the blue wing of the PL band. The detectivity drops rapidly at around 825 nm and results are not reliable from that point. Apart from that, we can see that high excitation raises PL of an unknown band at 650 nm. We should point out that **Fig. 4.5** is normalized so it shows the relative strength of the 650 nm band to the detected part of the main PL band. It must be stressed that we detect only the small part of the main band – even though it appears that SRO-B excited by the highest I_{exc} possesses a stronger 650 nm band than the main one, it is not the case. We will show later that this PL band decays moderately fast, for this reason, we will designate it as a fast red band (FRB).

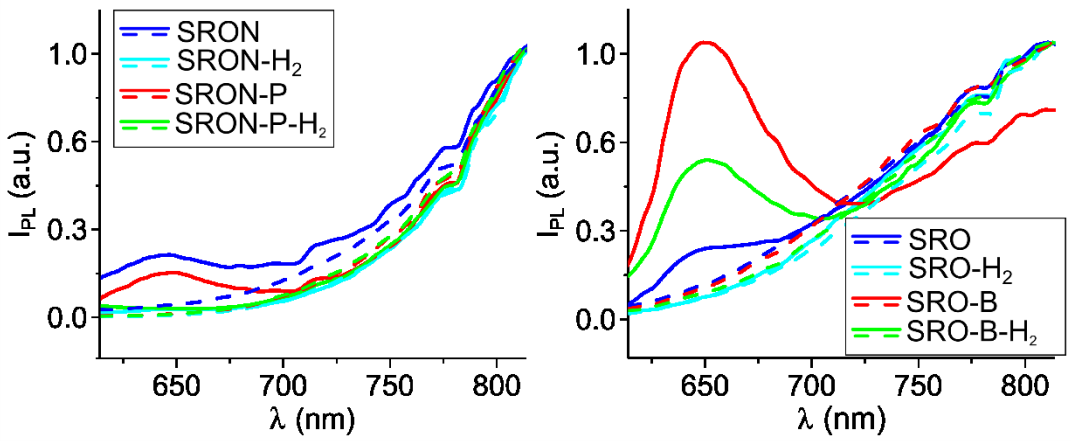

Fig. 4.5 Normalized PL spectra for I_{exc} = 100 mJ/cm^2 (solid lines) and 6 mJ/cm^2 (dashed lines) integrated over the time window of 0 – 100 μs.

To investigate further the origin of FRB we looked first at samples of NCs of different sizes. If there were a shift of PL band, then the PL would be influenced by quantum confinement and was connected to some internal states of NCs. Again we started with CW excitation. The results are in **Fig. 4.6a.** We looked at smaller NCs (3 nm) and larger ones (5 nm). We can see that the PL spectra of the main band shift as expected.

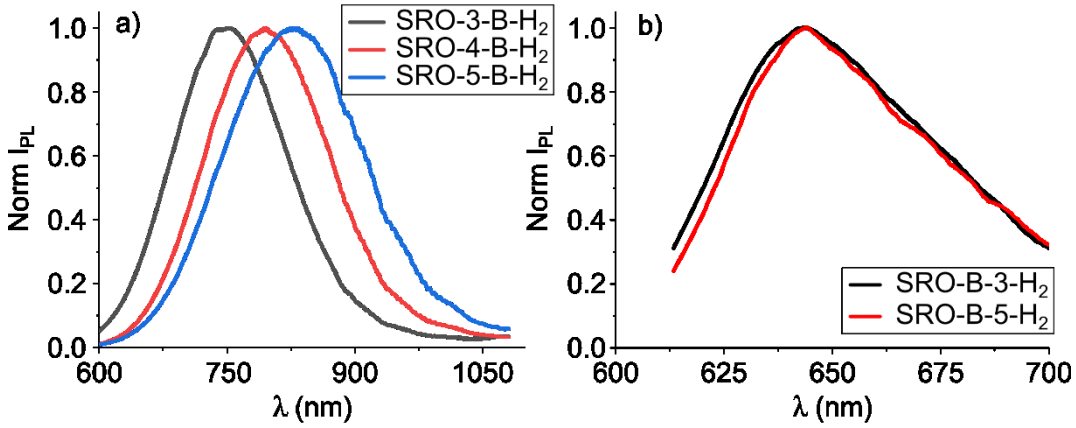

Fig. 4.6 a) PL spectra of the second sample set (**Table 4.2**). Samples were excited by a continuous HeCd laser, 325 nm, measured PL is thus time-integrated. b) Spectral position of the FRB for the two NC sizes, pulsed excitation.

Comparing the FRB spectra of 3 nm and 5 nm NCs (**Fig. 4.6b**) we can see the FRB does not shift at all. Analysis of smaller NCs is a bit problematic since the main PL band shifts too close to the FRB, but raising the I_{exc} sufficiently high shows FRB with minimal influence of the main PL band. Since FRB does not seem to be connected with the internal states of SiNC, we looked to the surface and/or matrix as the origin of FRB. As the matrix is SiO_2 we measured the SiO_2 layer (single layer with a width equivalent to the NC samples) without NCs and also the SiO_2 layer deposited in the presence of boron gas (due to the FRB being stronger in boron-doped measurements). The results are in **Fig. 4.7**. We can see that FRB is present and the inclusion of boron increases its PL. In SiO_2 the band position at the place of FRB is caused by a non-bridging oxygen hole center (NBOHC) defect [118]. The decay times are in tens of μs which is what we detected also in our samples.

To investigate the origin of FRB we measured the decay of this band (**Fig. 4.8**). The displayed results are limited just to the samples which show the highest PL of FRB and SiO_2. The decays are quite similar (apart from SRON) showing the same origin in all the samples. Considering that SRON and SRON-P samples show low intensity FRB, it seems that the inclusion of nitrogen in the matrix is detrimental to this PL band.

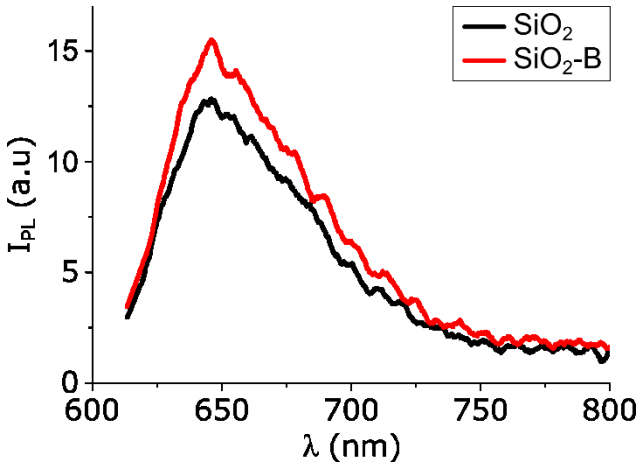

Fig. 4.7 PL spectra of references after the strong pulsed excitation.

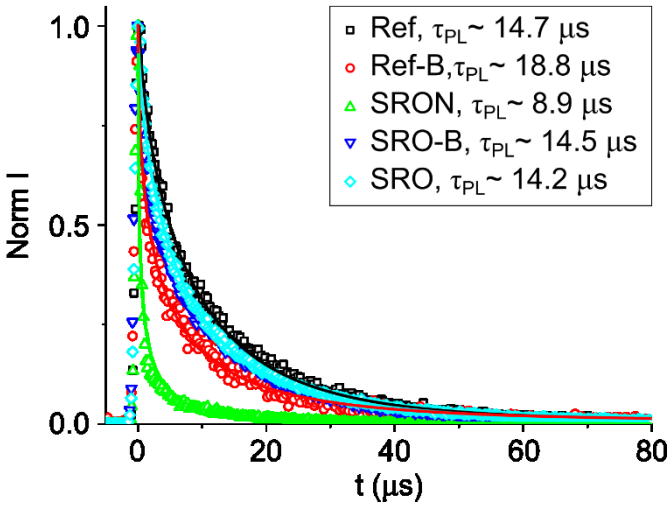

Fig. 4.8 Decays of the first sample set at 650nm. In the legend, the decay times are average decay lifetimes.

The decay is nonexponential. The best fit was achieved by the so-called stretched exponential function which can and is also used to fit the main PL band. This function was originally conceived to describe electric discharge in glasses by Rudolf Kohlrausch [119] (hence it is sometimes called Kohlrausch function in literature) and for PL decays was first used in 1907 by Werner [120]. The origins of the function reveal that it is used purely empirically without any fundamental connection to the PL process. But since the function was used to model processes in disordered systems, there were attempts to connect the β parameter to the level of disorder in SiNC samples. Especially as the very first samples were porous SiNC networks that possessed large distribution of NC sizes, surface quality, and distance between NCs. Theoretically, the single SiNCs should have then β = 1, i.e. have single-exponential decay, as other NC materials like CdS, CdSe. This is indeed the case [121], although there are large variations of decay times even for the same emission energies (presumably NCs with the same size). Another group measured PL on monodisperse, size-purified SiNCs [122] and obtained again stretched exponential decays. This shows the sensitivity of the SiNCs on their surroundings and small variations

of shape/ surface character. But the broad decay time distribution maybe also inherent due to the indirect gap as was proposed by Delerue [123]. The dispersion of electron and hole momentum due to the uncertainty principle enables recombination through multiple phonon channels which each has its own decay time. That would lead to fluctuations of decay on a single NC level leading to non-monoexponential decay times which does not seem to be the case. The monoexponential decay of single NCs holds for room temperature and transitions to biexponential for low temperatures [124]. Single NCs emit with one decay time which varies strongly between different nanocrystals even if they emit on the same energy. This variety of decay times leads to the sum of monoexponentials with different decay times which manifests in PL as stretched exponential [123].

In **Fig. 4.8**, the decay times written next to the particular sample are the so-called average decay lifetimes [125]. It is the average time it takes the excited carrier to recombine after being excited. The thusly defined decay time is independent of the used fitting model and is very useful in comparing different samples. Also, many times using a particular fitting model is based on preference than a particular physics reason, for example, typical decays of our samples could be fitted by stretched exponential or two-exponential decay models without significant difference. Thus the average decay lifetime is almost the same for both fitting models. Or in the case of stretched exponential decay, the decay time is strongly dependent on the Beta parameter and it is not straightforwardly clear how different betas change the decay curve.

The average decay lifetime $\bar{\tau}$ is calculated as follows:

$$\bar{\tau} = \frac{\int_0^\infty tI(t)\,\mathrm{d}t}{\int_0^\infty t\,\mathrm{d}t} \tag{4.2}$$

where *I(t)* is the detected PL. As can be seen, the definition of $\bar{\tau}$ (also intensity average lifetime) is independent of the fitting model and can also be calculated straight from the raw data. Considering a concrete fitting model enables us to

calculate the $\bar{\tau}$ from the fitting parameters. For two-exponential decay given as $I_{2exp}(t) = A_1 e^{-t/\tau_1} + A_2 e^{-t/\tau_2}$, $\bar{\tau}_{2exp}$ is calculated as follows:

$$\bar{\tau} = \frac{A_1\tau_1^2 + A_2\tau_2^2}{A_1\tau_1 + A_2\tau_2} \tag{4.3}$$

For stretched exponential given as $I_{SE}(t) = Ae^{-(t/\tau)^{\beta}}$, the calculation of $\bar{\tau}_{SE}$ is trickier [62] but results in:

$$\bar{\tau}_{SE} = \frac{\Gamma_f\left(\frac{2}{\beta}\right)}{\Gamma_f\left(\frac{1}{\beta}\right)}\tau \tag{4.4}$$

where β is the stretching (empirical) parameter and Γ_f the gamma function.

NBOHC is one of the most common defects in silica. Chemically it is the oxygen dangling bond – oxygen which is bonded to one silicon atom having only one electron in one of its non-bonding 2p orbitals. A schematic representation is in **Fig. 4.9**. Non-bridging means that the oxygen does not "connect" (bridge) two silicon atoms. In our system they are created probably during the formation of nanocrystals due to the mechanical strain on the Si/SiO_2 interface which splits the ≡Si - O - Si≡ bond into ≡Si-O•(NBOHC) and ≡Si•(E center) ([126], [127])

To analyze the FRB properly we tried to isolate it from the spectra. We use the spectrum measured with the lowest I_{exc}. There the influence of FRB wings on the PL of the main band is minimal. We then normalized the spectra measured with higher I_{exc} to the main band of the lowest I_{exc}. Then we can subtract the lowest I_{exc} spectrum from the other ones which isolates the FRB band from the rest of the spectra. In our range of I_{exc}, the shape of the main band did not change, only errors are given by the measurement noise. The exemplar result of this procedure is shown in **Fig. 4.10**.

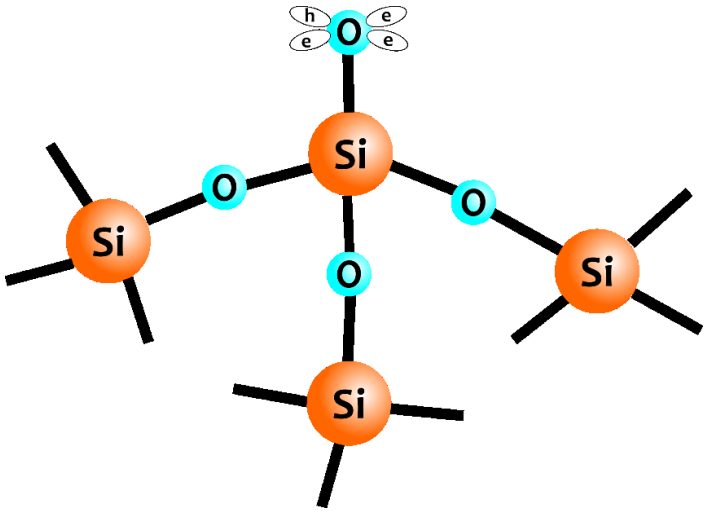

Fig. 4.9 Schematic representation of NBOHC.

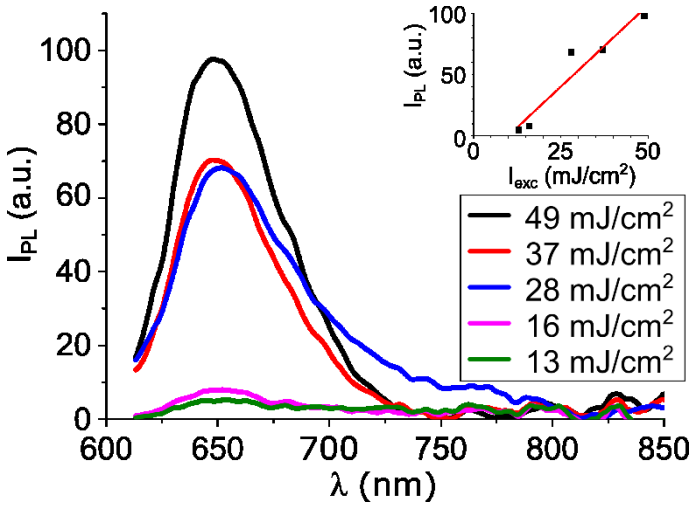

Fig. 4.10 The result of subtraction of the lowest intensity spectrum (6 mJ/cm^2) from spectra of higher excitation intensities which were normalized to the main band PL (this is the reason why this band is effectively zero in this figure). *Inset:* Dependence of FRB PL maximum on excitation intensity.

As can be seen in the insert of **Fig. 4.10**, the PL of FRB increases linearly with I_{exc} but also does not originate at zero. This points to faster decay channels which need to be saturated for the FRB PL to be detectable.

Repeating the measurements revealed some discrepancies which we looked closer into. Firstly, the PL of the main band lowers above some threshold

intensity while FRB PL increases linearly. Secondly, going from higher I_{exc} to lower the PL of FRB is higher compared to the other direction of changing I_{exc} as can be seen in **Fig. 4.11** where we show the dependence of I_{PL} on I_{exc} for SiO_2, SiO_2-B, SRO-3-B-H_2, and SRO-B-H_2.

Looking at the decays in **Fig. 4.12**, we can see that after application of high I_{exc} the decay times lower permanently. We will return to this fact in further discussion.

Comparing the results in **Fig. 4.11** we can see that FRB behaves similarly for both sets of samples (SiNCs and reference). But the FRB PL in NC samples is 2 magnitudes stronger than in reference signifying either a higher concentration of defects or some kind of energy transfer of excitation from NCs to NBOHC. What also points to an energy transfer is the enhancement of FRB PL in boron-doped SiNC samples which is also quite a bit higher than in the reference sample (i.e. the enhancement is not produced just by more NBOHC introduced by boron incorporation). To investigate this hypothesis we had to at least estimate the absolute efficiency of PL detection of our setup, i.e. how many photons emitted correspond to one count.

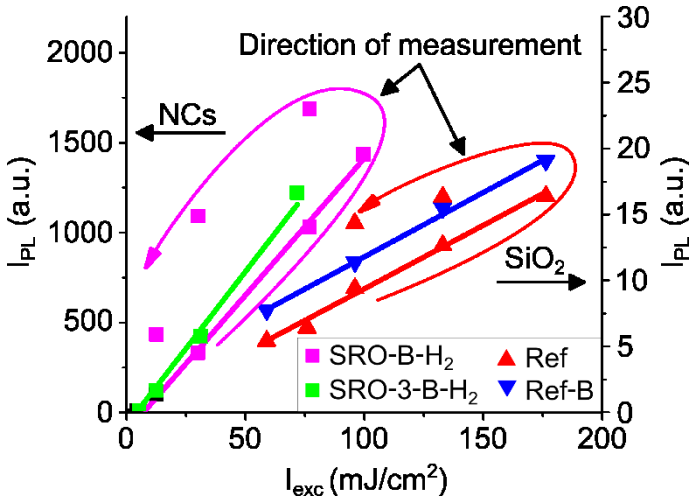

Fig. 4.11 The I_{exc} dependence of I_{PL}^{FRB} at 650 nm both for SiO_2 references and SiNCs; for SRO-B-H_2 and Ref we also show PL hysteresis (arrow shows the direction of the measurement).

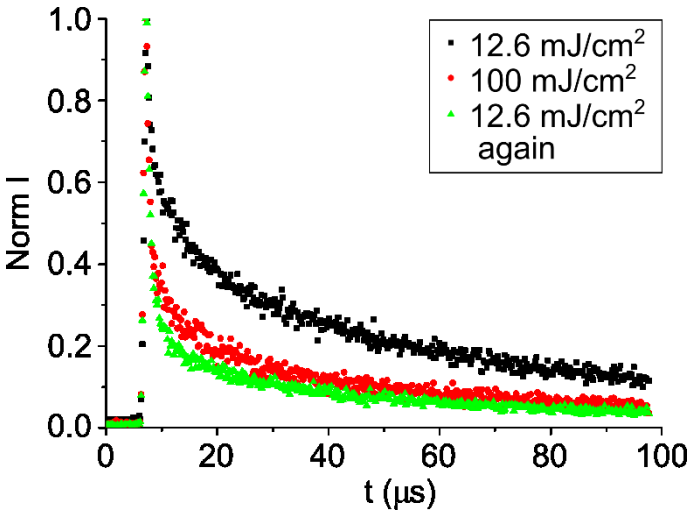

Fig. 4.12 Normalized PL decay curves of the FRB in SRO-5-B-H_2 for low, high, and a subsequent low I_{exc}.

That was possible due to the known quantum yield η of our samples [118]. If we can estimate PL intensity I_{PL} in absolute units, we can get from the following relation the number of excited NBOHC defects N_{NBOHC}:

$$I_{PL} = N_{NBOHC}\eta_{NBOHC} \tag{4.5}$$

where η_{NBOHC} is the quantum yield of NBOHC in our samples which we have estimated to be approximately 0.5. The radiative lifetime t_r of NBOHC strongly depends on its variant and can vary from 15 μs [128] to almost 4x times the number [129]. Compared to our PL lifetimes η determined as t_{PL}/t_r is at least 0.3. Not knowing the exact structure of NBOHC in our samples we decided on the average value of 0.5.

At maximum I_{exc} we found that in the area we collect PL from there are around 1×10^8 excited NBOHCs (in the SRO-B sample). That translates to roughly ¼ areal concentration of nanocrystals which is around 1×10^{12} cm^{-2} (areal concentration is used because NCs are deployed in 1 NC thick layers). The upward limit for NBOHC concentration is given by the lowest detectable FRB signal – considering only direct excitation (without any energy transfer)

absorption cross-section σ of NBOHC equal to 1.5×10^{-19} cm^2 [126], concentration cannot be higher than 2×10^{12} cm^{-2} which follows from:

$$I_{PL} = N_{NBOHC}\sigma\eta_{NBOHC}I_{exc} \tag{4.6}$$

This is a reasonable number since Pb(0) defect is the dominant defect in our samples with concentrations on the order of 10^{13} cm^{-2} [130], we would not expect other defects to have a higher concentration. We do not consider the influence of NBOHC in SiO_2 layers where the concentration is several orders lower as can be seen from I_{PL} of reference samples.

If we compare the estimate of PL due to direct excitation with detected PL of FRB, we can see that due to the energy transfer the PL increases which makes the absorption cross-section of NBOHC effectively as much as 40x higher. This actually corresponds to the ratio of FRB I_{PL} of SRO-B compared to Ref-B.

As can be seen in **Fig. 4.3**, the H_2- treatment had a severely adverse effect on FRB PL. H_2 treatment is applied to passivate non-radiative defects, particularly the dominant one Pb(0) mentioned above, on the interface of SiNCs and matrix they are incorporated in [131]. This also applies in our samples (doped or undoped), even though the boron-doped samples are not passivated completely – FRB is still detectable compared to others where it is completely quenched (or at least below detection limit). In our case, boron actually enhances luminescence of FRB, around 3-fold compared to untreated sample (SRO). It also somewhat shields some portion of NBOHC from H_2 passivation. The reason for this behavior might be the specific area the boron dopants incorporate into. Instead of being located inside the SiNCs (as are for example the P dopants [116]), they are spread over the SRO matrix and concentrated very close to the surface of the SiNCs [115]. They thus seem to mediate the energy transfer from SiNC core to NBOHC close to the surface. Phosphorus on the other hand deploys differently, as was noted above, and impairs the FRB PL.

4.5 The energy-transfer mechanism

As we have shown above, the energy transfer of excitation energy from SiNCs to NBOHCs plays a dominant role in FRB luminescence. Due to the otherwise low absorption cross-section of NBOHC at our excitation wavelength, the defects are not saturated even for high I_{exc}, when the samples get damaged and new NBOHCs are created.

What type of energy transfer mechanism could be possible? It must be quite fast (the temporal resolution of our streak camera is ~15 ps and we did not observe any slow rise). Also, it should have some energy activation threshold since it is observable for quite high I_{exc} and as was shown in **Fig. 4.10**, the I_{exc} dependence of I_{PL} for SiNC samples does not intercept the x-axis at zero.

We found the energy transfer mechanism with such characteristics in [107] where the authors describe energy transfer from Si nanocrystals to erbium ions mediated by hot electrons. The electrons need to have high enough excess energy to excite the NBOHC (the energy difference between the ground and excited state is at least 1.9 eV [129]). Our excitation wavelengths translate to the excitation energy of 3.61 eV which after subtracting the direct $\Gamma_{15} - \Gamma'_{25}$ bandgap energy of Si (3.4 eV in bulk at room temperature, slightly lower in NCs [96]). This leaves around 200 meV of excess energy which is clearly insufficient to excite NBOHC. But the "combination" of two such photons has enough energy to do that. The sufficiently hot-electron can be a result of for example generation of two excitons inside one nanocrystal. This results in Auger recombination where one exciton non-radiatively recombines transferring the energy to the other. The other mechanisms can be free-carrier absorption or two-photon excitation. We can safely exclude two-photon excitation since the I_{exc} dependence should then not be linear (sole two-photon results in quadratic dependence). The free-carrier absorption is weak in our spectral range but since our I_{exc} are quite high (4.2 mJ corresponds to an average

number of excitons per nanocrystal <N> = 3.8), it cannot be excluded completely. But it should not impact the linear dependence.

Due to the reasons given above, we believe that Auger recombination is the dominant process creating the hot electrons able to transfer the excess energy to NBOHC. It is a non-linear process in a way that the Auger recombination time depends cubically on the excess number of carriers. But since the PL lifetime in our samples is in tens of μs, compared to the ps speed of the Auger recombination it does not make a difference if the Auger recombination is faster or not. The resulting linear I_{exc} dependence of I_{PL} is thus strictly given by the number of hot carriers generated by the laser beam. The hot electron is delocalized and can easily interact with NBOHC in the SiNC vicinity. The range of such non-resonant interaction is necessarily limited and should not reach beyond 1.5 nm ([111], [132]). In the case of resonant transfer, the range can extend beyond 6 nm [133].

In our case, the distance between the particular SiNCs is given by SiNCs density and size since the SiNCs are created homogeneously [134]. The density was kept constant and given the size of nanocrystals to be 4.5 (3) nm, they are separated by around 2 (4) nm. So the highest distance of the NBOHC from NCs is around 3 nm (see **Fig. 4.13a**).

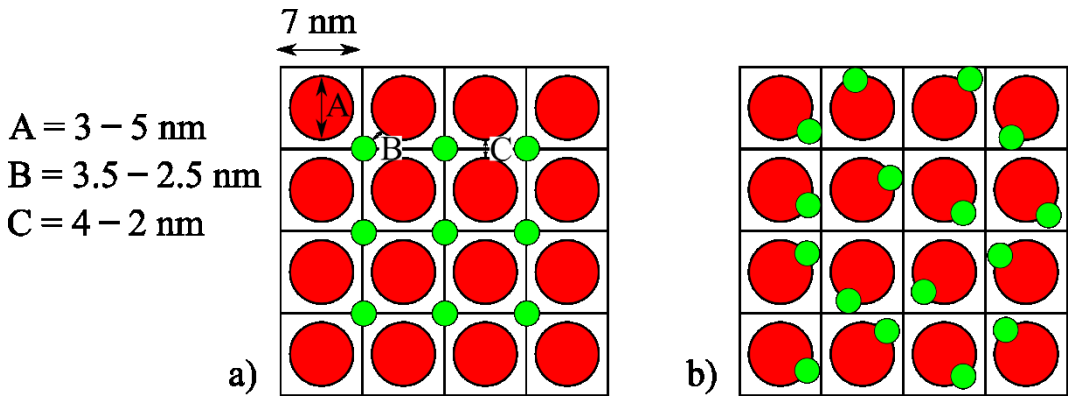

Fig. 4.13 a) Schematic distribution of NBOHC in a homogeneous case. b) Schematic distribution of NBOHC we consider more probable.

But we would expect the NBOHCs to be around matrix disruption, i.e. not homogeneously dispersed around the matrix but to be very close to the nanocrystals which are disrupting the SiO_2 matrix (**Fig. 4.13b**). The energy can then be transferred to a significant portion of them.

The transfer efficiency depends on the I_{exc}, in the best case measured scenario – at I_{exc} = 30 mJ/cm^2 after sample modification by high I_{exc} before – 1 excitation was transferred per 200 photons absorbed.

To summarize the energy transfer happens during or shortly after the excitation to the first excited state. It is mediated by hot electrons which are created through Auger recombination. It must be stressed that we use high excitation intensities up to the point of irreversible damage to the samples. The damage, in this case, means that the main band PL is decreased but actually the FRB PL is enhanced.

Not only it is enhanced, but also the FRB PL lifetime shortens permanently. Shortening of the PL lifetime is most of the time connected to shortening of the non-radiative lifetime which then leads to lower I_{PL} (that happens in our case for the main band). In the case of FRB where the I_{PL} raises, the radiative lifetime t_r must be shortened to produce such an effect – that follows from $\eta = t_{nr}/(t_{nr} + t_r)$. This effect could be caused by the rearrangement of bonds within the centers (as was noted above the decay time of NBOHC strongly depends on its variant) by high-intensity excitation. A similar effect was produced by controlled doping by phosphorus [135]. An increase in the radiative rate of highly excited SiNCs in solid matrices was also reported here [136].

Alternatively or rather concurrently, the high I_{exc} can create more NBOHCs which raises the I_{PL} naturally but would not modify the PL lifetime.

Another form of enhancement is given when boron is incorporated into the samples - those have the highest I_{PL} of FRB. This is probably due to the

particular location it concentrates in – it can be predominantly found in the suboxide shell surrounding the SiNC core. The energy states created in the bandgap of Si and SiO_2 [137] help the electron transfer from the nanocrystalline core. Our model is depicted in **Fig 4.14**.

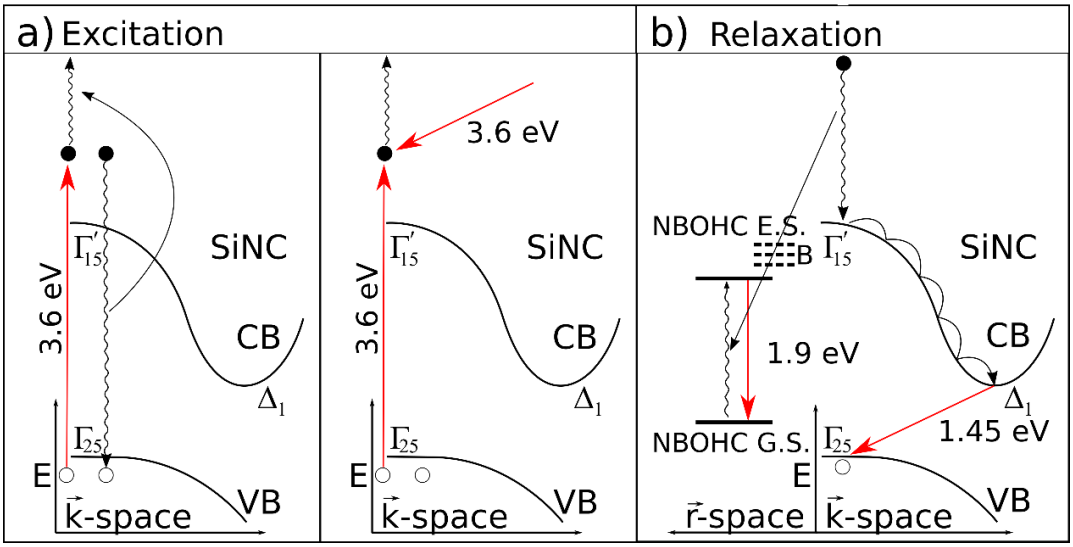

Fig. 4.14 Schematic energy level structure for the SiNCs samples. Straight red arrows display optical transitions while wavy arrows denote nonradiative relaxations and/or non-optical excitation. **a)** After sample excitation with high I_{exc} laser pulse, several electrons are elevated from valence band (VB) to conduction band (CB). There they can obtain more energy by Auger recombination (left panel) or free carrier absorption, i.e. absorption of another photon (right panel) **b)** Excess energy is transferred to the NBOHC resulting in its excitation. The electron then relaxes to the bottom of CB. Radiative recombination in the NC and NBOHC results in the main band PL and FRB PL, respectively. Boron-related states are depicted by dashed lines. E. S. denotes the excited state, G. S. the ground state.

We also investigated the dynamics of the main band PL more closely. Most of our samples behave as is usual for SiNCs. The PL can be fitted by stretched exponential and shows a common trend where the shorter PL wavelengths have shorter decay times. The dependence of decay times on emission energy E_{em} is exponential:

$$\tau \propto exp(-E_{em}/E_0) \tag{4.7}$$

where E_0 seems to be almost constant for different types of Si nanocrystals. It was theoretically determined to be 0.31 eV [123], and measured in SiNCs

produced by laser breakdown of SiH_4 [137] – value 0.3 eV, porous Si [138], SiNCs produced by non-thermal plasma [139] – both with value 0.25eV. This dependence follows from the combination of the indirect nature of Si bandgap and quantum confinement [123].

The dependence of decay times of our samples on emission energy is shown in **Fig. 4.15** and **Fig. 4.16**. The model above works well for SRON samples and undoped SRO samples (value of E_0 is between 0.21 – 0.29 eV) but for SRO-B samples the dependence is linear. For several samples, the low energy tail does not fit either linear or exponential decay dependence. Since our streak camera loses sensitivity rapidly in this region, the measured values are not that reliable, the discrepancies can be due to artifacts. Nevertheless, the linear dependence is rare and shows a rather profound effect on the distribution of density of states by boron and the role the localized surface states play in the main band PL.

We can also see that there is a clear dependence of decay times on the size of the nanocrystals and passivation. The bigger the NCs the shorter the decay times are. This can be explained by the fact that they are more prone to having defects quenching the luminescence than the smaller NCs. Passivation prolongs the decay times as can be expected.

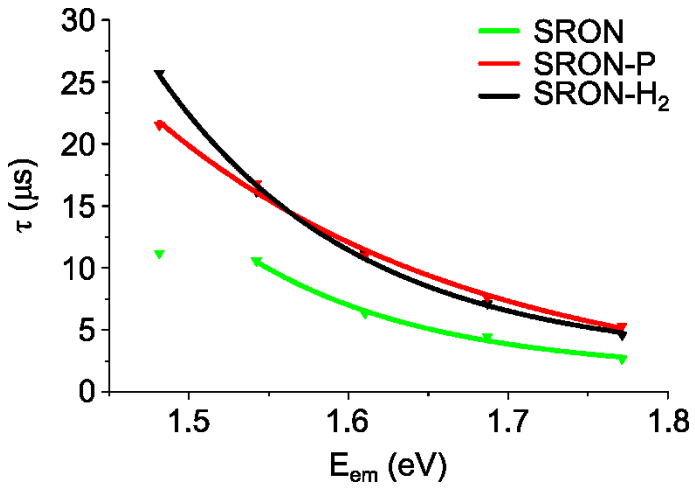

Fig. 4.15 Dependence of the PL decay times (from stretched exponential fits) on the emission energy for SRON samples. The lines are fits by an exponential function.

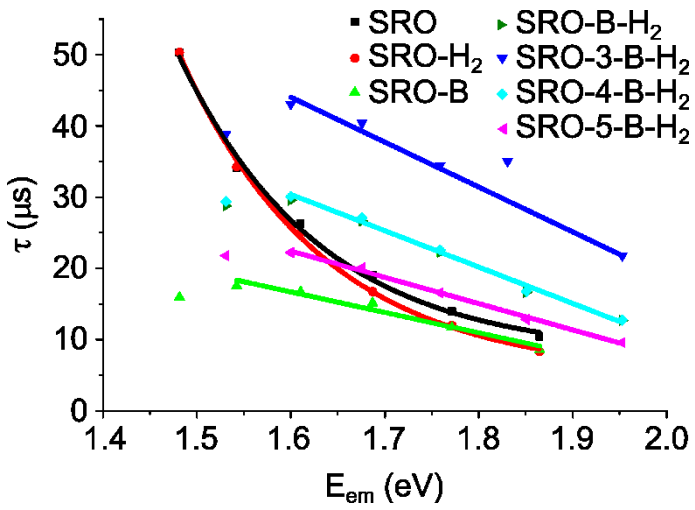

Fig. 4.16 The dependence of the decay times (from stretched exponential fits) on the emission energy for SRO samples. The lines are fits by exponential decay or linear function where appropriate.

Conclusion

In this chapter we described our experiments on the SiNCs in the form of superlattices which underwent several different treatments – annealing in the H_2 atmosphere to passivate defects and deposition in boron- or phosphorus-containing atmosphere. We found that these samples exhibit PL at 650 nm when strongly excited which we connected to the NBOHC defect. The PL of NBOHC is not only caused by direct excitation but mainly, especially for higher excitation intensities, by energy transfer from SiNCs which have much a higher absorption cross-section than NBOHC We also investigated the effect of boron and phosphorus on NBOHC PL. Phosphorus has an adverse effect on NBOHC PL, unlike boron which enhances the NBOHC PL considerably. It also partially shields the NBOHC against H_2 treatment which effectively passivates NBOHC (as it does other defects) in other samples. Very high excitation intensity creates more NBOHCs that increase the energy transfer efficiency, enhancing the PL of the 650 nm band. Should such PL be required the energy transfer efficiency can be maximized by engineering the samples with an optimal concentration of boron and NBOHC centers.

We have also found another effect of boron incorporation. It is well known that the dependence of PL lifetime on emission wavelength in SiNC is exponential which is connected to the quantum confinement influence on the density of states distribution. The dependence switches to linear when boron is added during deposition. This shows that even though boron does not incorporate into the SiNCs, it affects the distribution of density of states.

5 Conclusion

Semiconductors form the backbone of modern civilization. Their ubiquitous presence is given by the demand for smart control, connectivity, and power efficiency. The expansion to all areas of our life creates new obstacles for old materials and thus fresh opportunities for new ones.

As part of the work, we constructed the difference frequency generator which extended our experimental capabilities. We described the decision and construction steps needed in building such a setup and its inclusion in existing experimental infrastructure.

We then used the newly generated MIR pulses in the pump & probe setup to study the dynamics of the excited charge carriers in monocrystalline diamond. During the low-temperature measurements, we observed the dynamics of condensation into an electron-hole (e-h) liquid which leads to highly dense electron and hole populations. Their plasma frequency is roughly in the middle of our MIR range which enabled us to study the system with light above and below the plasma frequency. We confirmed that the system can be well described by the classical Drude theory of free carrier absorption in broad parameter space meaning that above the plasma frequency the response of the e-h system is dominated by absorption and the reflectivity plays a big role below. From our measurements, we determined the Drude scattering time in e h drops to be 12 fs and estimated their arrangement after condensation.

Moderate temperature measurements where e-h condensation does not take place revealed new dynamics feature when the probe wavelength was sufficiently long, in our case 8 μm. We employed the quantum theory of free carrier absorption to prove that this component is connected to thermalisation of charged carriers mainly through acoustic (and not optical) phonons. From our measurements, this thermalisation occurs on a time scale of 40 ps. Also dominance of scattering on acoustic phonons channel in the free carrier

absorption results in roughly quadratic wavelength dependence which also validates the use of classical theory.

In the second part of this thesis, we measured the time-resolved photoluminescence of Si nanocrystals in the form of superlattices differing in size and preparation process, especially samples that had incorporated boron or phosphorus. After strong excitation, we detected a previously unobserved emission band at 650 nm which we connected to the presence of a non-bridging oxygen center. We found that this defect is not only excited directly but mainly through energy transfer from the more efficiently excited Si nanocrystals. We also investigated the influence of boron, phosphorus, and hydrogen on this defect. Hydrogen and to lesser extent phosphorus effectively passivate this defect resulting in no detectable photoluminescence. On the other hand, boron enhances its emission and decreases the effectivity of hydrogen passivation. We connected this enhancement tentatively to higher energy transfer efficiency since the boron incorporates to the surface of nanocrystals where these centers are located. We also found that high enough excitation intensity causes shortening of radiative decay time in the centers.

As the last point, we investigated the dependence of photoluminescence decay time on the emission wavelength. The conventional exponential dependence connected to the quantum confinement influence on the density of states distribution was observed in all samples apart from the ones with boron incorporated. There the dependence was strictly linear showing that the influence of boron on Si nanocrystals is more profound than previously thought.

References

[1] Hamamatsu, "Operating principle of streak camera," *Retrieved from https://www.hamamatsu.com/eu/en/product/photometry-systems/streak-camera/operating-principle/index.html*. .

[2] Y. Yao, A. J. Hoffman, and C. F. Gmachl, "Mid-infrared quantum cascade lasers," *Nat. Photonics*, vol. 6, no. 7, pp. 432–439, Jul. 2012.

[3] M. Tacke, "Lead–salt lasers," *Philos. Trans. R. Soc. London. Ser. A Math. Phys. Eng. Sci.*, vol. 359, no. 1780, pp. 547–566, Mar. 2001.

[4] C. R. Petersen *et al.*, "Mid-infrared supercontinuum covering the 1.4-13.3 μm molecular fingerprint region using ultra-high NA chalcogenide step-index fibre," *Nat. Photonics*, vol. 8, no. 11, pp. 830–834, 2014.

[5] R. W. Boyd, *Nonlinear optics*, 7th ed. San Diago, CA: Academic Press, 2003.

[6] M. Born *et al.*, *Principles of Optics*. Cambridge University Press, 1999.

[7] T. Popelář, F. Trojánek, M. Kozák, and P. Malý, "Dynamics of photoexcited carriers in CVD diamond studied by mid-infrared femtosecond spectroscopy," *Diam. Relat. Mater.*, vol. 71, pp. 13–19, Jan. 2017.

[8] S. Koizumi, M. Kamo, Y. Sato, H. Ozaki, and T. Inuzuka, "Growth and characterization of phosphorous doped {111} homoepitaxial diamond thin films," *Appl. Phys. Lett.*, vol. 71, no. 8, pp. 1065–1067, Aug. 1997.

[9] J. Mort *et al.*, "Boron doping of diamond thin films," *Appl. Phys. Lett.*, vol. 55, no. 11, pp. 1121–1123, Sep. 1989.

[10] K. Liu, J. Chu, C. Johnston, and S. Roth, "Measurement of electrical activation energy in boron-doped diamond using the flatband capacitance method," *J. Appl. Phys.*, vol. 83, no. 8, pp. 4202–4205, Apr. 1998.

[11] I. Stenger *et al.*, "Impurity-to-band activation energy in phosphorus doped diamond," *J. Appl. Phys.*, vol. 114, no. 7, p. 073711, 2013.

[12] C. J. H. Wort and R. S. Balmer, “Diamond as an electronic material,” *Mater. Today*, vol. 11, no. 1–2, pp. 22–28, Jan. 2008.

[13] J. Isberg *et al.*, “High carrier mobility in single-crystal plasma-deposited diamond,” *Science (80-.).*, vol. 297, no. 5587, pp. 1670–1672, Sep. 2002.

[14] N. Donato, N. Rouger, J. Pernot, G. Longobardi, and F. Udrea, “Diamond power devices: state of the art, modelling, figures of merit and future perspective,” *J. Phys. D. Appl. Phys.*, vol. 53, no. 9, p. 093001, Feb. 2020.

[15] H. Umezawa, S. Shikata, and T. Funaki, “Diamond Schottky barrier diode for high-temperature , high-power , and fast switching applications,” vol. 06, pp. 6–10.

[16] J.-H. Seo *et al.*, “Thermal diffusion boron doping of single-crystal natural diamond,” *J. Appl. Phys.*, vol. 119, no. 20, p. 205703, May 2016.

[17] “Diamond wafer technologies for semiconductor device applications,” in *Power Electronics Device Applications of Diamond Semiconductors*, Elsevier, 2018, pp. 1–97.

[18] F. P. Bundy, “Direct Conversion of Graphite to Diamond in Static Pressure Apparatus,” *Science (80-.).*, vol. 137, no. 3535, pp. 1057–1058, Sep. 1962.

[19] K. Nassau and J. Nassau, “The history and present status of synthetic diamond,” *J. Cryst. Growth*, vol. 46, no. 2, pp. 157–172, Feb. 1979.

[20] S. Koizumi, “Ultraviolet Emission from a Diamond pn Junction,” *Science (80-.).*, vol. 292, no. 5523, pp. 1899–1901, Jun. 2001.

[21] A. Oh, “Diamond particle detectors systems in high energy physics,” *J. Instrum.*, vol. 10, no. 04, pp. C04038–C04038, Apr. 2015.

[22] N. Naka, K. Fukai, Y. Handa, and I. Akimoto, “Direct measurement via cyclotron resonance of the carrier effective masses in pristine diamond,” *Phys. Rev. B*, vol. 88, no. 035205, pp. 1–5, 2013.

[23] J. R. Chelikowsky and S. G. Louie, “First-principles linear combination of atomic orbitals method for the cohesive and structural properties of solids:

Application to diamond," *Phys. Rev. B*, vol. 29, no. 6, pp. 3470–3481, Mar. 1984.

[24] P. J. Dean, E. C. Lightowlers, and D. R. Wight, "Intrinsic and Extrinsic Recombination Radiation from Natural and Synthetic Aluminum-Doped Diamond," *Phys. Rev.*, vol. 140, no. 1A, pp. A352–A368, Oct. 1965.

[25] L. V. Keldysh, "No Title," in *Proceedings of the 9th International Conference on Physics of Semiconductors*, 1968, pp. 1303–1312.

[26] J. R. Haynes, "Experimental Observation of the Excitonic Molecule," *Phys. Rev. Lett.*, vol. 17, no. 16, pp. 860–862, Oct. 1966.

[27] W. F. Brinkman and T. M. Rice, "Electron-Hole Liquids in Semiconductors," *Phys. Rev. B*, vol. 7, no. 4, pp. 1508–1523, Feb. 1973.

[28] R. Sauer, N. Teofilov, and K. Thonke, "Exciton condensation in diamond," *Diam. Relat. Mater.*, vol. 13, no. 4–8, pp. 691–699, Apr. 2004.

[29] M. Willatzen, M. Cardona, and N. E. Christensen, "Linear muffin-tin-orbital and k · p calculations of effective masses and band structure of semiconducting diamond," *Phys. Rev. B*, vol. 50, no. 24, pp. 18054–18059, Dec. 1994.

[30] I. Pelant and J. Valenta, "Highly excited semiconductors," in *Luminescence Spectroscopy of Semiconductors*, Oxford University Press, 2012, pp. 205–241.

[31] M. A. Vouk, "Conditions necessary for the formation of the electron-hole liquid in diamond and calculation of its parameters," *J. Phys. C Solid State Phys.*, vol. 12, no. 12, pp. 2305–2312, Jun. 1979.

[32] K. Thonke *et al.*, "Electron–hole drops in synthetic diamond," *Diam. Relat. Mater.*, vol. 9, no. 3–6, pp. 428–431, Apr. 2000.

[33] M. Nagai, R. Shimano, K. Horiuchi, and M. Kuwata-Gonokami, "Creation of supercooled exciton gas and transformation to electron-hole droplets in diamond," *Phys. Rev. B*, vol. 68, no. 8, p. 081202, Aug. 2003.

[34] N. Teofilov, R. Schliesing, K. Thonke, H. Zacharias, R. Sauer, and H. Kanda, "Optical high excitation of diamond: phase diagram of excitons, electron–hole

liquid and electron–hole plasma," *Diam. Relat. Mater.*, vol. 12, no. 3–7, pp. 636–641, Mar. 2003.

[35] N. Naka, J. Omachi, and M. Kuwata-Gonokami, "Suppressed formation of electron-hole droplets in diamond under a strain field," *Phys. Rev. B*, vol. 76, no. 19, p. 193202, Nov. 2007.

[36] J. Omachi, N. Naka, K. Yoshioka, and M. Kuwata-gonokami, "Enhanced Formation of Electron-Hole Droplets in Diamond by a Weak Pulse Injection," in *Conference on Lasers and Electro-Optics/Quantum Electronics and Laser Science Conference and Photonic Applications Systems Technologies*, 2008, p. JWA117.

[37] M. Kozák, F. Trojánek, T. Popelář, and P. Malý, "Control of condensation and evaporation of electron-hole liquid in diamond by femtosecond laser pulses," *Phys. status solidi - Rapid Res. Lett.*, vol. 7, no. 4, pp. 278–281, Apr. 2013.

[38] M. Nagai, R. Shimano, K. Horiuch, and M. Kuwata-Gonokami, "Phase diagram of the quantum degenerate electron-hole system in diamond," *Phys. Status Solidi Basic Res.*, vol. 238, no. 3, pp. 509–512, 2003.

[39] P. Drude, "Zur Elektronentheorie der Metalle," *Ann. Phys.*, vol. 306, no. 3, pp. 566–613, 1900.

[40] M. E. Thomas, "Multiphonon model for absorption in diamond," 1994, vol. 2286, pp. 152–159.

[41] J. Walker, "Optical absorption and luminescence in diamond," *Reports Prog. Phys.*, vol. 42, no. 10, pp. 1605–1659, Oct. 1979.

[42] R. B. Hammond and R. N. Silver, "Onsets of the Electron-Hole-Droplet Luminescence in Si," *Phys. Rev. Lett.*, vol. 42, no. 8, pp. 523–526, Feb. 1979.

[43] A. Fujii, K. Takiyama, R. Maki, and T. Fujita, "Lifetime and quantum efficiency of luminescence due to indirect excitons in a diamond," *J. Lumin.*, vol. 94–95, pp. 355–357, Dec. 2001.

[44] Y. Kubo, S. Temgoua, R. Issaoui, J. Barjon, and N. Naka, "Radiative lifetime of boron-bound excitons in diamond," *Appl. Phys. Lett.*, vol. 114, no. 13, p.

132104, Apr. 2019.

[45] M. Kozák, F. Trojánek, and P. Malý, “Large prolongation of free-exciton photoluminescence decay in diamond by two-photon excitation,” *Opt. Lett.*, vol. 37, no. 11, p. 2049, Jun. 2012.

[46] R. Shimano, M. Nagai, K. Horiuch, and M. Kuwata-Gonokami, “Formation of a High Tc Electron-Hole Liquid in Diamond,” *Phys. Rev. Lett.*, vol. 88, no. 5, p. 057404, Jan. 2002.

[47] J. H. Jiang, M. W. Wu, M. Nagai, and M. Kuwata-Gonokami, “Formation and decay of electron-hole droplets in diamond,” *Phys. Rev. B*, vol. 71, no. 3, p. 035215, Jan. 2005.

[48] M. Kozák, F. Trojánek, T. Popelář, and P. Malý, “Dynamics of electron–hole liquid condensation in CVD diamond studied by femtosecond pump and probe spectroscopy,” *Diam. Relat. Mater.*, vol. 34, pp. 13–18, Apr. 2013.

[49] M. Kozák, F. Trojánek, and P. Malý, “Temperature and density dependence of exciton dynamics in IIa diamond: Experimental and theoretical study,” *Phys. status solidi*, vol. 211, no. 10, pp. 2244–2250, Oct. 2014.

[50] M. Kozák, F. Trojánek, and P. Malý, “Hot-carrier transport in diamond controlled by femtosecond laser pulses,” *New J. Phys.*, vol. 17, no. 5, p. 053027, May 2015.

[51] W. P. Dumke, “Quantum Theory of Free Carrier Absorption,” *Phys. Rev.*, vol. 124, no. 6, pp. 1813–1817, Dec. 1961.

[52] K. Seeger, *Semiconductor Physics*, Springer s., vol. 40. Berlin, Heidelberg: Springer Berlin Heidelberg, 1991.

[53] C. Jacoboni and L. Reggiani, “The Monte Carlo method for the solution of charge transport in semiconductors with applications to covalent materials,” *Rev. Mod. Phys.*, vol. 55, no. 3, pp. 645–705, 1983.

[54] S. Koizumi, C. Nebel, and M. Nesladek, Eds., *Physics and Applications of CVD Diamond*. Weinheim, Germany: Wiley-VCH Verlag GmbH & Co. KGaA, 2008.

[55] J. Hammersberg *et al.*, “Stability of polarized states for diamond valleytronics,” *Appl. Phys. Lett.*, vol. 104, no. 23, p. 232105, Jun. 2014.

[56] M. Nesladek, A. Bogdan, W. Deferme, N. Tranchant, and P. Bergonzo, “Charge transport in high mobility single crystal diamond,” *Diam. Relat. Mater.*, vol. 17, no. 7–10, pp. 1235–1240, 2008.

[57] T. Malinauskas, K. Jarašiūnas, E. Ivakin, N. Tranchant, and M. Nesladek, “Determination of carrier diffusion coefficient and lifetime in single crystalline CVD diamonds by light-induced transient grating technique,” *Phys. status solidi*, vol. 207, no. 9, pp. 2058–2063, Sep. 2010.

[58] K. Ishioka, M. Hase, M. Kitajima, and H. Petek, “Coherent optical phonons in diamond,” *Appl. Phys. Lett.*, vol. 89, no. 23, p. 231916, 2006.

[59] T. Popelář, L. Ondič, I. Pelant, K. Kůsová, and D. Hiller, “Energy transfer channel between silicon nanocrystals and an optical center emitting above their bandgap,” *J. Lumin.*, vol. 215, no. August, p. 116685, 2019.

[60] H. Takagi, H. Ogawa, Y. Yamazaki, A. Ishizaki, and T. Nakagiri, “Quantum size effects on photoluminescence in ultrafine Si particles,” *Appl. Phys. Lett.*, vol. 56, no. 24, pp. 2379–2380, Jun. 1990.

[61] L. T. Canham, “Silicon quantum wire array fabrication by electrochemical and chemical dissolution of wafers,” *Appl. Phys. Lett.*, vol. 57, no. 10, pp. 1046–1048, Sep. 1990.

[62] O. King and D. G. Hall, “Impurity-related photoluminescence from silicon at room temperature,” *Phys. Rev. B*, vol. 50, no. 15, pp. 10661–10665, Oct. 1994.

[63] M. A. Tischler, R. T. Collins, J. H. Stathis, and J. C. Tsang, “Luminescence degradation in porous silicon,” *Appl. Phys. Lett.*, vol. 60, no. 5, pp. 639–641, Feb. 1992.

[64] T. Yoshida, S. Takeyama, Y. Yamada, and K. Mutoh, “Nanometer-sized silicon crystallites prepared by excimer laser ablation in constant pressure inert gas,” *Appl. Phys. Lett.*, vol. 68, no. 13, pp. 1772–1774, Mar. 1996.

[65] K. Abderrafi *et al.*, “Silicon Nanocrystals Produced by Nanosecond Laser

Ablation in an Organic Liquid," *J. Phys. Chem. C*, vol. 115, no. 12, pp. 5147–5151, Mar. 2011.

[66] V. Švrček, J.-L. Rehspringer, E. Gaffet, A. Slaoui, and J.-C. Muller, "Unaggregated silicon nanocrystals obtained by ball milling," *J. Cryst. Growth*, vol. 275, no. 3–4, pp. 589–597, Mar. 2005.

[67] C. M. Hessel *et al.*, "Hydrogen Silsesquioxane : A Molecular Precursor for Nanocrystalline Si - SiO 2 Composites and Freestanding Hydride-Surface-Terminated Silicon Nanoparticles," no. 1, pp. 6139–6146, 2006.

[68] J. A. Kelly, E. J. Henderson, and J. G. C. Veinot, "Sol–gel precursors for group 14 nanocrystals," *Chem. Commun.*, vol. 46, no. 46, p. 8704, 2010.

[69] U. Kortshagen, "Nonthermal plasma synthesis of semiconductor nanocrystals," *J. Phys. D. Appl. Phys.*, vol. 42, no. 11, p. 113001, Jun. 2009.

[70] T. Shimizu-Iwayama, T. Hama, D. E. Hole, and I. W. Boyd, "Characteristic photoluminescence properties of Si nanocrystals in SiO2 fabricated by ion implantation and annealing," *Solid. State. Electron.*, vol. 45, no. 8, pp. 1487–1494, Aug. 2001.

[71] M. Zacharias, J. Heitmann, R. Scholz, U. Kahler, M. Schmidt, and J. Bläsing, "Size-controlled highly luminescent silicon nanocrystals: A SiO/SiO2 superlattice approach," *Appl. Phys. Lett.*, vol. 80, no. 4, pp. 661–663, Jan. 2002.

[72] D. C. Hannah, J. Yang, N. J. Kramer, G. C. Schatz, U. R. Kortshagen, and R. D. Schaller, "Ultrafast Photoluminescence in Quantum-Confined Silicon Nanocrystals Arises from an Amorphous Surface Layer," *ACS Photonics*, vol. 1, no. 10, pp. 960–967, Oct. 2014.

[73] K. Kůsová, L. Ondič, and I. Pelant, "Comment on 'Ultrafast Photoluminescence in Quantum-Confined Silicon Nanocrystals Arises from an Amorphous Surface Layer,'" *ACS Photonics*, vol. 2, no. 3, pp. 454–455, Mar. 2015.

[74] B. V. Oliinyk, D. Korytko, V. Lysenko, and S. Alekseev, "Are Fluorescent Silicon Nanoparticles Formed in a One-Pot Aqueous Synthesis?," *Chem.*

Mater., vol. 31, no. 18, pp. 7167–7172, 2019.

[75] J. L. Wilbrink, C.-C. Huang, K. Dohnalova, and J. M. J. Paulusse, "Critical assessment of wet-chemical oxidation synthesis of silicon quantum dots," *Faraday Discuss.*, vol. 222, pp. 149–165, 2020.

[76] A. Gupta, M. T. Swihart, and H. Wiggers, "Luminescent Colloidal Dispersion of Silicon Quantum Dots from Microwave Plasma Synthesis: Exploring the Photoluminescence Behavior Across the Visible Spectrum," *Adv. Funct. Mater.*, vol. 19, no. 5, pp. 696–703, Mar. 2009.

[77] M. V. Wolkin, J. Jorne, P. M. Fauchet, G. Allan, and C. Delerue, "Electronic states and luminescence in porous silicon quantum dots: The role of oxygen," *Phys. Rev. Lett.*, vol. 82, no. 1, pp. 197–200, 1999.

[78] M. Dasog, G. B. De Los Reyes, L. V. Titova, F. A. Hegmann, and J. G. C. Veinot, "Size vs Surface: Tuning the Photoluminescence of Freestanding Silicon Nanocrystals Across the Visible Spectrum via Surface Groups," *ACS Nano*, vol. 8, no. 9, pp. 9636–9648, 2014.

[79] M. Miyano *et al.*, "Photophysical properties of luminescent silicon nanoparticles surface-modified with organic molecules via hydrosilylation," *Photochem. Photobiol. Sci.*, vol. 15, no. 1, pp. 99–104, 2016.

[80] G. M. Carroll, R. Limpens, and N. R. Neale, "Tuning Confinement in Colloidal Silicon Nanocrystals with Saturated Surface Ligands," *Nano Lett.*, vol. 18, no. 5, pp. 3118–3124, 2018.

[81] C. Qian *et al.*, "Non-wettable, Oxidation-Stable, Brightly Luminescent, Perfluorodecyl-Capped Silicon Nanocrystal Film," *J. Am. Chem. Soc.*, vol. 136, no. 45, pp. 15849–15852, Nov. 2014.

[82] K. Dohnalová, T. Gregorkiewicz, and K. Kůsová, "Silicon quantum dots: Surface matters," *J. Phys. Condens. Matter*, vol. 26, no. 17, 2014.

[83] K. Kůsová *et al.*, "Direct Bandgap Silicon: Tensile-Strained Silicon Nanocrystals," *Adv. Mater. Interfaces*, vol. 1, no. 2, p. 1300042, Apr. 2014.

[84] A. N. Poddubny and K. Dohnalová, "Direct band gap silicon quantum dots

achieved via electronegative capping," *Phys. Rev. B - Condens. Matter Mater. Phys.*, vol. 90, no. 24, pp. 1–7, 2014.

[85] A. N. Thiessen *et al.*, "Silicon Nanoparticles: Are They Crystalline from the Core to the Surface?," *Chem. Mater.*, vol. 31, no. 3, pp. 678–688, 2019.

[86] Y. Okada and Y. Tokumaru, "Precise determination of lattice parameter and thermal expansion coefficient of silicon between 300 and 1500 K," *J. Appl. Phys.*, vol. 56, no. 2, pp. 314–320, Jul. 1984.

[87] J. R. Chelikowsky and M. L. Cohen, "Electronic structure of silicon," *Phys. Rev. B*, vol. 10, no. 12, pp. 5095–5107, Dec. 1974.

[88] T.-Y. Kim *et al.*, "Quantum confinement effect of silicon nanocrystals in situ grown in silicon nitride films," *Appl. Phys. Lett.*, vol. 85, no. 22, pp. 5355–5357, Nov. 2004.

[89] J. P. Proot, C. Delerue, and G. Allan, "Electronic structure and optical properties of silicon crystallites: Application to porous silicon," *Appl. Phys. Lett.*, vol. 61, no. 16, pp. 1948–1950, Oct. 1992.

[90] S. Ögüt, J. R. Chelikowsky, and S. G. Louie, "Quantum confinement and optical gaps in si nanocrystals," *Phys. Rev. Lett.*, vol. 79, no. 9, pp. 1770–1773, 1997.

[91] P. Hapala, K. Kůsová, I. Pelant, and P. Jelínek, "Theoretical analysis of electronic band structure of 2- to 3-nm Si nanocrystals," *Phys. Rev. B*, vol. 87, no. 19, p. 195420, 2013.

[92] K. Kůsová *et al.*, "Direct Bandgap Silicon: Tensile-Strained Silicon Nanocrystals," *Adv. Mater. Interfaces*, vol. 1, no. 2, p. 1300042, Apr. 2014.

[93] A. A. Prokofiev *et al.*, "Direct bandgap optical transitions in Si nanocrystals," *JETP Lett.*, vol. 90, no. 12, pp. 758–762, 2010.

[94] F. Sangghaleh, I. Sychugov, Z. Yang, J. G. C. Veinot, and J. Linnros, "Near-Unity Internal Quantum Efficiency of Luminescent Silicon Nanocrystals with Ligand Passivation," *ACS Nano*, vol. 9, no. 7, pp. 7097–7104, 2015.

[95] J. Valenta *et al.*, “Nearly perfect near-infrared luminescence efficiency of Si nanocrystals : A comprehensive quantum yield study employing the Purcell effect,” no. June, pp. 1–9, 2019.

[96] W. D. A. M. De Boer *et al.*, “Red spectral shift and enhanced quantum efficiency in phonon-free photoluminescence from silicon nanocrystals,” *Nat. Nanotechnol.*, vol. 5, no. 12, pp. 878–884, 2010.

[97] D. Timmerman, J. Valenta, K. Dohnalová, W. D. A. M. De Boer, and T. Gregorkiewicz, “Step-like enhancement of luminescence quantum yield of silicon nanocrystals,” *Nat. Nanotechnol.*, vol. 6, no. 11, pp. 710–713, 2011.

[98] M. Govoni, I. Marri, and S. Ossicini, “Carrier multiplication between interacting nanocrystals for fostering silicon-based photovoltaics,” *Nat. Photonics*, vol. 6, no. 10, pp. 672–679, 2012.

[99] L. Pavesi and G. Guillot, Eds., *Optical Interconnects*, vol. 119. Berlin, Heidelberg: Springer Berlin Heidelberg, 2006.

[100] H. Nishimura *et al.*, “Biocompatible fluorescent silicon nanocrystals for single-molecule tracking and fluorescence imaging,” *J. Cell Biol.*, vol. 202, no. 6, pp. 967–983, Sep. 2013.

[101] B. F. P. McVey *et al.*, “Synthesis, optical properties and theoretical modelling of discrete emitting states in doped silicon nanocrystals for bioimaging,” *Nanoscale*, vol. 10, no. 33, pp. 15600–15607, 2018.

[102] A. D. Durnev *et al.*, “Evaluation of Genotoxicity and Reproductive Toxicity of Silicon Nanocrystals,” *Bull. Exp. Biol. Med.*, vol. 149, no. 4, pp. 445–449, Oct. 2010.

[103] L. M. Kustov *et al.*, “Silicon nanoparticles: characterization and toxicity studies,” *Environ. Sci. Nano*, vol. 5, no. 12, pp. 2945–2951, 2018.

[104] M. N. Obrovac and L. Christensen, “Structural Changes in Silicon Anodes during Lithium Insertion/Extraction,” *Electrochem. Solid-State Lett.*, vol. 7, no. 5, p. A93, 2004.

[105] M. Locritani *et al.*, “Silicon nanocrystals functionalized with pyrene units:

Efficient light-harvesting antennae with bright near-infrared emission," *J. Phys. Chem. Lett.*, vol. 5, no. 19, pp. 3325–3329, 2014.

[106] L. Ravotto *et al.*, "Bright Long-Lived Luminescence of Silicon Nanocrystals Sensitized by Two-Photon Absorbing Antenna," *Chem*, vol. 2, no. 4, pp. 550–560, 2017.

[107] A. Lesage, D. Timmerman, D. M. Lebrun, Y. Fujiwara, and T. Gregorkiewicz, "Hot-carrier-mediated impact excitation of Er^{3+} ions in SiO_2 sensitized by Si Nanocrystals," *Appl. Phys. Lett.*, vol. 113, no. 3, p. 031109, 2018.

[108] B. Bruhn, B. J. Brenny, S. Dekker, I. Doğan, P. Schall, and K. Dohnalová, "Multi-chromatic silicon nanocrystals," *Light Sci. Appl.*, vol. 6, no. 6, p. e17007, 2017.

[109] A. R. Wilkinson and R. G. Elliman, "Kinetics of H2 passivation of Si nanocrystals in SiO2," *Phys. Rev. B*, vol. 68, no. 15, p. 155302, Oct. 2003.

[110] A. M. Hartel *et al.*, "Formation of size-controlled silicon nanocrystals in plasma enhanced chemical vapor deposition grown SiOxNy/SiO2 superlattices," *Thin Solid Films*, vol. 520, no. 1, pp. 121–125, 2011.

[111] J. Valenta, M. Greben, S. Gutsch, D. Hiller, and M. Zacharias, "Effects of inter-nanocrystal distance on luminescence quantum yield in ensembles of Si nanocrystals," *Appl. Phys. Lett.*, vol. 105, no. 24, 2014.

[112] J. W. Luo, P. Stradins, and A. Zunger, "Matrix-embedded silicon quantum dots for photovoltaic applications: A theoretical study of critical factors," *Energy Environ. Sci.*, vol. 4, no. 7, pp. 2546–2557, 2011.

[113] S. Godefroo *et al.*, "Classification and control of the origin of photoluminescence from Si nanocrystals," *Nat. Nanotechnol.*, vol. 3, no. 3, pp. 174–178, 2008.

[114] J. Valenta, M. Greben, Z. Remeš, S. Gutsch, D. Hiller, and M. Zacharias, "Determination of absorption cross-section of Si nanocrystals by two independent methods based on either absorption or luminescence," *Appl. Phys. Lett.*, vol. 108, no. 2, p. 023102, Jan. 2016.

[115] D. Hiller *et al.*, “Boron-Incorporating Silicon Nanocrystals Embedded in SiO2: Absence of Free Carriers vs. B-Induced Defects,” *Sci. Rep.*, vol. 7, no. 1, p. 8337, Dec. 2017.

[116] D. Hiller, J. López-Vidrier, S. Gutsch, M. Zacharias, K. Nomoto, and D. König, “Defect-Induced Luminescence Quenching vs. Charge Carrier Generation of Phosphorus Incorporated in Silicon Nanocrystals as Function of Size,” *Sci. Rep.*, vol. 7, no. 1, p. 863, Dec. 2017.

[117] D. Hiller *et al.*, “Absence of free carriers in silicon nanocrystals grown from phosphorus- and boron-doped silicon-rich oxide and oxynitride,” *Beilstein J. Nanotechnol.*, vol. 9, pp. 1501–1511, May 2018.

[118] L. Skuja, “Optically active oxygen-deficiency-related centers in amorphous silicon dioxide,” *J. Non. Cryst. Solids*, vol. 239, no. 1–3, pp. 16–48, 1998.

[119] R. Kohlrausch, “Theorie des elektrischen Rückstandes in der Leidener Flasche,” *Ann. der Phys. und Chemie*, vol. 167, no. 2, pp. 179–214, 1854.

[120] A. Werner, “Quantitative Messungen der An- und Abklingung getrennter Phosphorescenzbanden,” *Ann. Phys.*, vol. 24, p. 164, 1907.

[121] F. Sangghaleh, B. Bruhn, T. Schmidt, and J. Linnros, “Exciton lifetime measurements on single silicon quantum dots,” 2013.

[122] S. L. Brown, R. Krishnan, A. Elbaradei, J. Sivaguru, M. P. Sibi, and E. K. Hobbie, “Origin of stretched-exponential photoluminescence relaxation in size-separated silicon nanocrystals,” *AIP Adv.*, vol. 7, no. 5, 2017.

[123] C. Delerue, G. Allan, C. Reynaud, O. Guillois, G. Ledoux, and F. Huisken, “Multiexponential photoluminescence decay in indirect-gap semiconductor nanocrystals,” *Phys. Rev. B - Condens. Matter Mater. Phys.*, vol. 73, no. 23, pp. 1–4, 2006.

[124] F. Pevere, F. Sangghaleh, B. Bruhn, I. Sychugov, and J. Linnros, “Rapid Trapping as the Origin of Nonradiative Recombination in Semiconductor Nanocrystals,” *ACS Photonics*, vol. 5, pp. 2990–2996, 2018.

[125] M. Greben, P. Khoroshyy, I. Sychugov, and J. Valenta, “Non-exponential

decay kinetics: correct assessment and description illustrated by slow luminescence of Si nanostructures," *Appl. Spectrosc. Rev.*, vol. 54, no. 9, pp. 758–801, Oct. 2019.

[126] G. Vaccaro, "Structural Modification Processes in Bulk and Nano-sized Amorphous SiO2 Systems," *Thesis*, 2011.

[127] R. A. Weeks and E. Sonder, "in," in *Paramagnetic Resonance, Vol. 2*, W. Low, Ed. New York: Academic Press, 1963, p. 869.

[128] L. Vaccaro, M. Cannas, and R. Boscaino, "Luminescence features of nonbridging oxygen hole centres in silica probed by site-selective excitation with tunable laser," *Solid State Commun.*, vol. 146, no. 3–4, pp. 148–151, 2008.

[129] L. Vaccaro, M. Cannas, V. Radzig, and R. Boscaino, "Luminescence of the surface nonbridging oxygen hole center in silica: Spectral and decay properties," *Phys. Rev. B - Condens. Matter Mater. Phys.*, vol. 78, no. 7, pp. 1–6, 2008.

[130] D. Hiller, M. Jivanescu, A. Stesmans, and M. Zacharias, "Pb (0) centers at the Si-nanocrystal/ SiO2 interface as the dominant photoluminescence quenching defect," *J. Appl. Phys.*, vol. 107, no. 8, 2010.

[131] S. Cheylan and R. G. Elliman, "Effect of particle size on the photoluminescence from hydrogen passivated Si nanocrystals in SiO2," *Appl. Phys. Lett.*, vol. 78, no. 13, pp. 1912–1914, 2001.

[132] K. Imakita, M. Fujii, and S. Hayashi, "The mechanism of energy transfer from Si nanocrystals to Er ions in SiO2 : Different mechanisms depending on Er concentration," *Eur. Phys. J. D*, vol. 34, no. 1–3, pp. 161–163, 2005.

[133] H. Sugimoto, K. Furuta, and M. Fujii, "Controlling Energy Transfer in Silicon Quantum Dot Assemblies Made from All-Inorganic Colloidal Silicon Quantum Dots," *J. Phys. Chem. C*, vol. 120, no. 42, pp. 24469–24475, 2016.

[134] J. Laube, S. Gutsch, D. Wang, C. Kübel, M. Zacharias, and D. Hiller, "Two-dimensional percolation threshold in confined Si nanoparticle networks," *Appl. Phys. Lett.*, vol. 108, no. 4, 2016.

[135] V. A. Belyakov and V. A. Burdov, “Γ-X mixing in phosphorus-doped silicon nanocrystals: Improvement of photon generation efficiency,” *Phys. Rev. B - Condens. Matter Mater. Phys.*, vol. 79, no. 3, pp. 1–9, 2009.

[136] E. M. L. D. De Jong *et al.*, “Thermally stimulated exciton emission in Si nanocrystals,” *Light Sci. Appl.*, vol. 7, no. 1, pp. 17133–17137, 2018.

[137] Y. Kanemitsu, “Luminescence properties of nanometer-sized Si crystallites: Core and surface states,” *Phys. Rev. B*, vol. 49, no. 23, pp. 16845–16848, 1994.

[138] D. Amans, O. Guillois, G. Ledoux, D. Porterat, and C. Reynaud, “Influence of light intensity on the photoluminescence of silicon nanostructures,” *J. Appl. Phys.*, vol. 91, no. 8, pp. 5334–5340, Apr. 2002.

[139] M. Greben, P. Khoroshyy, X. Liu, X. Pi, and J. Valenta, “Fully radiative relaxation of silicon nanocrystals in colloidal ensemble revealed by advanced treatment of decay kinetics,” *J. Appl. Phys.*, vol. 122, no. 3, 2017.

List of Figures

List of Tables

List of abbreviations

AGS	Silver Thiogallate ($AgGaS_2$)
CVD	Chemical vapor deposition
DFG	Difference-frequency generation
EHL	Electron-hole liquid
FCA	Free carrier absorption
FC	Free carrier
FE	Free exciton
FRB	Fast red band
MCT	Mercury Cadmium Telluride (HgCdTe)
HPHT	High-pressure high-temperature
MIR	Mid-infrared
NBOHC	Non-bridging oxygen hole center
NC	Nanocrystal
PECVD	Plasma enhanced chemical vapor deposition
PL	Photoluminescence
P&p	Pump and probe
TRPL	Time-resolved photoluminescence

Author's publications

Results of the thesis were published in these articles:

T. Popelář, F. Trojánek, M. Kozák, and P. Malý, "Dynamics of photoexcited carriers in CVD diamond studied by mid-infrared femtosecond spectroscopy," *Diam. Relat. Mater.*, vol. 71, pp. 13–19, Jan. 2017

T. Popelář, L. Ondič, I. Pelant, K. Kůsová, and D. Hiller, "Energy transfer channel between silicon nanocrystals and an optical center emitting above their bandgap," *J. Lumin.*, vol. 215, no. August, p. 116685, 2019

Other articles published during the work on the thesis:

M. Kozák, F. Trojánek, T. Popelář, and P. Malý, "Control of condensation and evaporation of electron-hole liquid in diamond by femtosecond laser pulses," *Phys. status solidi - Rapid Res. Lett.*, vol. 7, no. 4, pp. 278–281, Apr. 2013

M. Kozák, F. Trojánek, T. Popelář, and P. Malý, "Dynamics of electron–hole liquid condensation in CVD diamond studied by femtosecond pump and probe spectroscopy," *Diam. Relat. Mater.*, vol. 34, pp. 13–18, Apr. 2013.

K. Kůsová and T. Popelář, "On the importance of onset times and multiple-wavelength analysis of photoluminescence decays," *J. Appl. Phys.*, vol. 125, no. 19, p. 193103, May 2019